High-throughput three-dimensional characterization of morphogenetic signals during the formation of the vertebrate retina

Mario Ledesma-Terrón[a,b,c], Diego Pérez-Dones[a,b,c], Diego Mazó-Durán[a,b],
David G. Míguez[a,b,d]

[a]*Depto de Fisica de la Materia Condensada, Universidad Autonoma de Madrid, Calle de Francisco Tomas y Valiente, 1, Madrid, 28049, Comunidad de Madrid, Spain*
[b]*Centro de Biologia Molecular Severo Ochoa, Universidad Autonoma de Madrid, Calle de Nocolas Cabrera, 1, Madrid, 28049, Comunidad de Madrid, Spain*
[c]*Equally contributing authors*
[d]*Corresponding author: david.miguez@uam.es*

Abstract

The precise differentiation of neural progenitors during development ensures the correct cognitive, sensory and motor functions of higher organisms. This balance between self-renewal and terminal differentiation is regulated by a complex interplay of signaling pathways, that set the spatial and temporal cues that ultimately shape and organize neurogenic tissues. The developing vertebrate retina is a widely used model to study how these key signaling cascades modulate the mode and rate of division of neural progenitors, despite its complex three-dimensional architecture and the asymmetric differentiation dynamics. Here, we present a comprehensive multi-step framework that integrates *in toto* experiments with three dimensional image analysis and theoretical tools to provide a quantitative characterization of the dynamics of growth and differentiation of the developing vertebrate retina. Additionally, we use small molecule inhibitors to show that Hh and FGF activation promote differentiation and cell cycle progression, while Wnt and Notch activation respectively increase and decrease the average division rate. These results represent a detailed and accurate quantitative characterization of the development and regulation of the vertebrate retina. We propose that the same framework can be directly used to characterize other *in vitro* or *in vivo* tissues.

Keywords: Neurogenesis, Morphogenesis, Image Processing, Organogenesis
PACS: 87.57.Q-, 87.57.cp, 87.57.nf
2000 MSC: 92C55, 68U10, 92C40

1. Introduction

Cells sense, interpret and respond to changes in their environment. Precise interpretation of these external signals during development ensures the appropriate structure, dimensions, and composition of adult tissues and organs. Failure

in this process can lead to important developmental disorders. The study of the complex interplay between these intracellular and extracellular cues is arguably one of the most frequently addressed topics in the field of Developmental Biology.

The developing retina is the most accessible portion of the vertebrates Central Nervous System, and an ideal organ for studying the dynamics and regulation of organogenesis in the context of neuronal differentiation. The basic processes involved in the formation of the vertebrate retina and the specification of its various neuronal sub-types are well characterized. In brief, a population of retinal progenitor cells (RPCs) gives rise to several types of terminally differentiated neurons that are produced sequentially: retinal ganglion cells are generated first and occupy the innermost layer; the two types of photoreceptors are next in line, followed by bipolar, horizontal and amacrine cells [1, 2].

Despite its apparent simplicity in spatial and temporal organization, several key aspects of the morphogenesis and regulation of the vertebrate retina remain unclear: how proliferation and differentiation of the pool of RPCs is balanced during retinal development?; how this balance is regulated by key regulatory signals in both space and time?; how the cell cycle of RPCs is modulated as the organ develops?; how is the interplay between cell cycle and differentiation during retinal formation?.

A prevalent methodology for investigating the morphogenesis of the developing retina is the use of representative sections of the tissue. Unfortunately, the highly asymmetric structure of the retina prevents the use of a single section to represent the entire tissue [3], so quantification must be performed using full three-dimensional information. Furthermore, given that dynamics is an integral part in any developmental process, a comprehensive characterization of neurogenesis in the developing retina should incorporate the temporal dimension. Unfortunately, characterization at single-cell resolution of densely packed cellular structures in four dimensions is challenging, due to reduced resolution or signal-to-noise ratio of 3D time-lapse movies performed *in vivo*.

To address these limitations, we devised a multi-step framework that combines experiments, image analysis, modeling and theoretical tools to obtain a quantitative characterization of the dynamics of growth and differentiation in developing tissues. Taking advantage of the three-dimensional information, nonlinear fitting algorithms and statistical analysis, we are able to bypass segmentation errors and produce highly accurate digital representations of dense 3D tissues.

Applied to the developing vertebrate retina, our analysis shows that the total number of cells increases exponentially during the first wave of neurogenesis, while balancing the changes in the number of RPCs and terminally differentiated neurons. We also demonstrate quantitatively how the average mode of division gradually shifts from proliferative to differentiative, concomitant with a reduction in average cell cycle length. Comparison of these data with embryos where Hh, Wnt, Notch, and FGF signaling are inhibited shows that both Hh and FGF promote differentiation and cell cycle progression, while Wnt and Notch respectively accelerate and decelerate the cell cycle.

2. Results

2.1. Object Statistical Clustering of Adjacent Regions (OSCAR) designed for realistic biological three-dimensional images.

Automated analysis and quantification of biological images rely on accurate segmentation. Many free and commercial software solutions can reliably identify individual cells in images with optimal signal-to-background ratio but fail in conditions of reduced resolution typical of images from dense three-dimensional samples. Additionally, typical 3D digital reconstructions of biological tissues from confocal sections are highly asymmetric, with two axes of high resolution, and a vertical Z axis with much less information that typically depends on the number of confocal sections and pinhole (see Supplementary Figure 1). Unfortunately, 3D segmentation relies in information in all spatial dimensions, so this axis of lowest resolution is the one that ultimately limits the segmentation accuracy in 3D [3].

With these limitations in mind, we have developed an Object Statistical Clustering of Adjacent Regions (OSCAR) framework specifically designed to perform accurate quantitative characterization in three-dimensional images from densely packed biological samples. In brief, OSCAR utilizes an in-house combination of arithmetic, geometric, and statistical algorithms to overcome segmentation errors caused by low signal-to-noise ratio or an axis of reduced resolution (details of the workflow are summarized in Methods and Supplementary Information).

To assess the capabilities of OSCAR and compare its accuracy with other free and commercial software solutions (see Supplementary Information), we utilize computer generated "ground truth" 3D images with asymmetric (Fig. 1A-D) or symmetric (fig. 1E) reduction in resolution (see Supplementary Information). When, focusing on the number of detected objects (Fig. 1F), all tools perform well under conditions of high signal-to-background ratio (radius of deformation, r_z=0). However, as the signal-to-background ratio decreases, OSCAR is able to perform with an accuracy above 80%, compared to 50% accuracy in the other tools (detecting twice or half the real number of objects in the image). OSCAR also outperforms (90% accuracy) the other solutions when the signal-to-background is uniformly reduced (Fig. 1G).

To assess the accuracy of OSCAR in spatial object detection in a 3D space, we developed an algorithm based on the Friedmann-Rafsky test (illustrated in Fig. 1H, explained in Supplementary Information). Results are plotted in Fig. 1I (shorter columns indicate smaller displacement, and therefore higher detection accuracy). As expected, accuracy for all tools tested is reduced as the signal-to-background ratio decreases. OSCAR (blue bar) outperforms the other tools when resolution is reduced directionally ($r_z = 8$ and $r_z = 12$), but not when image resolution is uniformly reduced ($r_x = r_y = r_z$). However, accuracy in the number of objects detected under this condition was much more precise in OSCAR compared to the other tools tested (Fig. 1G).

Furthermore, we tested OSCAR using three-dimensional projections of a developing zebrafish retina imaged *in toto* (Figure 1J, nuclei stained with ToPro3)
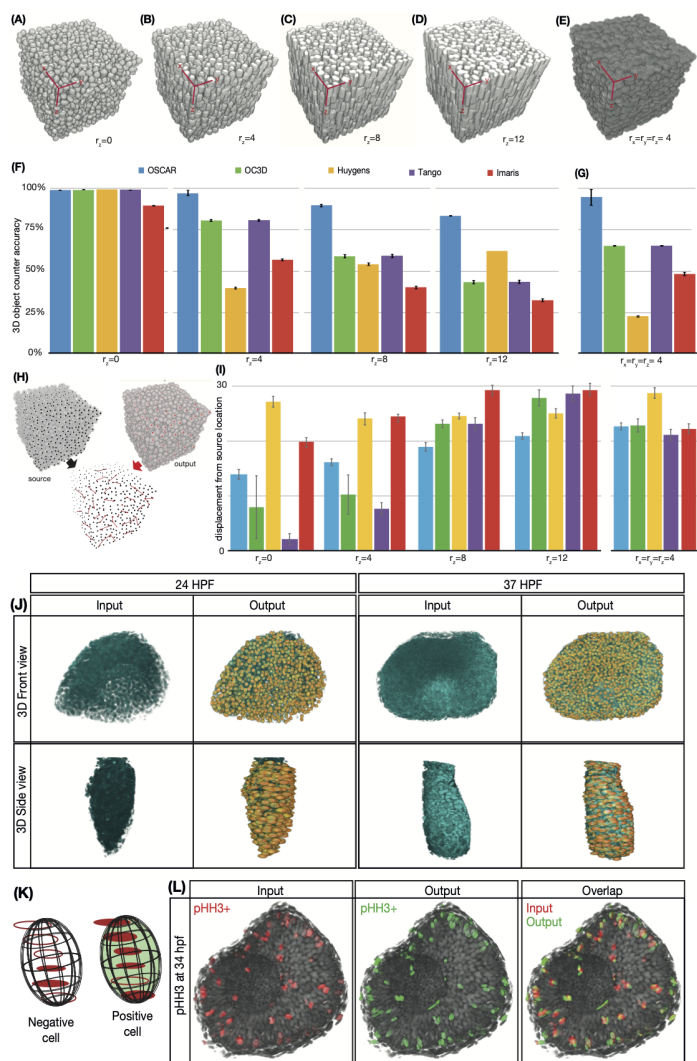
Figure 1: **OSCAR can localize and identify objects in conditions of reduced signal-to-noise ratio**. (A-E) Three-dimensional reconstruction of a set of computer generated "ground truth" images with 2500 cells, after image processing is applied to reduce signal-to-background ratio in one axis (radius of deformation (A) $r_z=0$, (B) $r_z=4$, (C) $r_z=8$ and (D) $r_z=12$) or in all three axis ($r_x = r_y = r_z=4$). (F-G) Accuracy in object quantification in the "ground truth" images above for different software solutions. (H) Scheme of the Friedmann-Rafsky test algorithm used to quantify localization accuracy. (I) Quantification of accuracy in the spatial localization of objects in the "ground truth" images above for different software solutions. (J) 3D projections of developing zebrafish retinas at 24 and 37 hpf (blue) used as input (nuclei staining with Topro3). Adjacent to each image, we plot the corresponding digital reconstructions generated by drawing the output nuclei as orange ellipsoids. (K) Scheme of how the framework uses others channels of the image to establish nuclei identity. (L) Left panel: 3D image projection of a zebrafish retina at 37 hpf stained with nuclear marker Topro3 (grey) and pHH3 immunofluorescence (red). Central panel: pHH3+ cells detected by OSCAR (green) are plotted on top of the nuclei channel. Right panel: pHH3+ cells detected by OSCAR (green) are plotted on top of input image to illustrate detection accuracy. Error bars in (F-G) represent the standard deviation between quantification of three different images. Error bars in (I) represent the standard deviation between three independent runs of the test.

at 24 and 37 hours post fertilization (hpf). The output was then used to generate 3D digital reconstructions, which are superimposed (in orange) on top of the input image (blue) to illustrate the performance and accuracy in terms of size and shape of the tissue.

Subsequently, capitalizing OSCAR's precision in locating individual cells (refer to Fig. 1I), we try to identify features based on variations in protein expression levels at the single cell level. A scheme of how this is implemented is depicted in Figure 1K (see Supplementary Information for a more detailed explanation). Figure 1L shows 3D image of a zebrafish retina at 34 hpf imaged *in toto*, wherein nuclear staining (ToPro3, grey) is combined with Phospho-histone H3 (pHH3) immunostaining (highlighting mitotic cells) in red. Details for the *in toto* immunofluorescence, specimen mounting and imaging procedures can be found in the Methods section. The output and overlay images (fig. 1L central and left panel) illustrate the overall good accuracy of the tool in terms of establishing cell identity.

In conclusion, our framework can accurately identify and locate objects in three-dimensional images with high object density and reduced signal-to-background ratio. When applied to 3D confocal reconstructions, such as images of the developing zebrafish retina, OSCAR reliably quantifies and locates individual nuclei. Compared to other software tools for 3D segmentation, OSCAR demonstrates superior accuracy under conditions typical of *in toto* 3D tissue samples and/or *in vivo* time lapse movies, where resolution and signal-to-background ratio are compromised.

2.2. The developing zebrafish retina grows linearly in volume and exponentially in cell numbers, resulting in an increase in cell density.

Next, the tool is used to characterize the growth and development of the developing zebrafish retina in the four dimensions (three dimensions + time). To do that, we proceed as follows (illustrated in Supplementary Figure 2): wild-type embryos are permitted to develop under standard conditions and are subsequently fixed at various hpf; they are then processed, cleared, stained and mounted using in-house developed protocols; tissues are imaged *in toto* using a confocal microscope. Finally, images are processed and analyzed using OSCAR (detailed protocols for each step can be found in the Methods section).

Examples of input images (2D sections and 3D projections) at three different hpf and stained with ToPro3 are shown in Fig. 2A. Corresponding digital reconstructions are displayed below, portraying detected cells as ellipsoids with shape, volume and location in the 3D space provided by OSCAR. The total number of cells detected for 14 time points (ranging from 20 to 48 hpf) is plotted in Fig. 2B. The dynamics fits well to an exponential growth pattern (blue line), while quantification of the total volume occupied by the retina (Fig. 2C) exhibits a temporal evolution that aligns well with a linear plot (details of the algorithm to find the best fit are explained in the Supplementary Information).

The combination of 3X increase (linear) in volume (Fig. 2C) and 8X increase (exponential) in cell numbers (Fig. 2B) results in a net rise in cell density as the retina develops. This value is estimated using two independent methods.
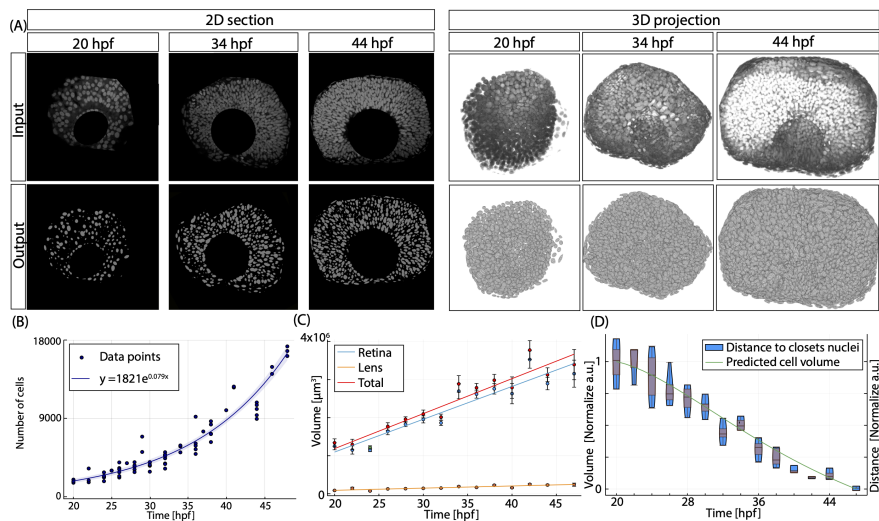
Figure 2: **The developing zebrafish retina grows exponentially in terms of cell numbers and linearly in terms of volume**. (A) Input confocal sections and 3D reconstructions of developing zebrafish retinas at different time points stained with ToPro3. Below each image the corresponding output representation is displayed (cells are drawn as ellipsoids with dimensions and location for each cell provided by OSCAR). (B) Plot of the total number of cells at different hpf (at least three independent repeats per time point). Data is fitted to an exponential function. Error bars represent the standard error of the mean value between repeats. (C) Estimation of volume occupied by the retina and lens at different hpf. Error bars represent the standard error of the mean value between repeats. (D) Boxplot of the average distance between 5-closest neighbors. Line represents the change in volume per cell measured as the fitting for number of cells divided by the fitting for the volume of the retina.

Firstly, we use the output of OSCAR to calculate the average distance of each cell in the tissue to its five closest neighbors at each time point. Then, we determine the volume per cell by dividing the linear change in volume of the retina (Fig. 2C, blue line) by the exponential fit in the total number of cells (Fig. 2B, blue line). Normalized results from packaging (boxplot in Fig. 2D) and average cell volume estimation (blue line in Fig. 2D) exhibit a similar trend, suggesting that our tool accurately detects the changes in form and organization occurring during retinal development. In conclusion, our data reveals a well-defined exponential growth of the developing zebrafish retina in terms of cell numbers, linear growth in volume, and an overall increase in cell density.

2.3. The average cell cycle shortens as differentiation increases during the first wave of neurogenesis.

Next, we capitalize on OSCAR's ability to establish cell identity based on differential proteins expression (see Figure 1 K-L) to quantify the dynamics of the first wave of neurogenesis in the developing zebrafish retina, in terms of the mode (proliferation versus differentiation) and the rate of divisions (length of cell cycle). To do that, embryos of the Tg(atoh7:GFP) line (engineered to express

GFP as a reporter for Atoh7 expression) are harvested at different hpf, fixed, and stained *in toto* with ToPro3 and immunostaining against Sox2, a transcription factor that plays an essential role in the maintenance of both embryonic and adult neural progenitors [4]. Subsequently, multi-channel images are acquired *in toto* and 3D confocal reconstructions are processed with OSCAR (sections, 3D projections and the corresponding digital reconstructions from OSCAR for three developmental stages are depicted in Fig. 3A).

Comparison of GFP and Sox2 normalized intensities at the single-cell level is then computed to classify cells into three categories (see Supplementary Figure 3A): nuclei positive for Sox2 and negative for Atoh7, nuclei negative for Sox2 and positive for Atoh7, and a small but non-negligible subset of cells positive for both Sox2 and Atoh7. To further identify these sets, we include immunofluorescence against Pcna (Supplementary Figure 3B-C) at three different hours post-fertilization (hpf). We observe that the vast majority of Sox2+/Atoh7- cells are Pcna+, allowing us to safely classify them as cycling progenitors. Conversely, the subset of Atoh7+/Sox2- cells are clearly Pcna-, allowing us to classify them as terminally differentiated [5].

To characterize the subset of Sox2+/Atoh7+ cells, we conducted immunofluorescence against pHH3 at three different hpf (Supplementary Figure 3D-E). We observe that some Sox2+/Atoh7+ are also pHH3+, indicating that certain cells initiating Atoh7 expression are are still actively cycling (Supplementary Figure 3E, yellow bars), consistent with prior research [6, 5]. The percentage of GFP+ cells that are also pHH3+ (Supplementary Figure 3E, purple bars) appears to remain consistent across various developmental stages. Furthermore, recent studies suggest that neurogenic progenitors emerging from asymmetric divisions express Atoh7, resembling intermediate progenitors identified in the mammalian neocortex [7].

Based on this, we have devised an automated labeling algorithm to categorize each cell type as follows (detailed in the Supplementary information and depicted in Fig. 3B): each cell is labeled as either progenitor **P** or differentiated **D** based on whether the number of pixels above threshold in the Sox2 channel is higher ($V_j^{Sox2} > V_j^{GFP}$) or lower ($V_j^{Sox2} < V_j^{GFP}$) than in the GFP channel, respectively. Cells exhibiting similar levels for both markers ($V_j^{Sox2} \approx V_j^{GFP}$) are designated as intermediate progenitors *IP*, in accordance with the aforementioned considerations.

The output of the algorithm for over 60 full retinas harvested at various hpf (Figure 3C) reveals that initially, approximately 100% of the cells are labeled as progenitors (*P*, orange). As time progresses, the percentage of cells in the tissue identified as terminally differentiated (*D*, green) increases, as well as the number of cells identified as positive for both markers also increases (representing around 20% of all cells at later stages).

Focusing on morphological differences, differentiated cells exhibit in average smaller nuclei compared to progenitors cells, with statistical significance (fig. 3D left panel, quantified for a a single image at 44 hpf for consistency). Moreover, the nuclei of differentiated cells are more homogeneous in size, again with high

7

statistical significance. Notably, no important differences in sphericity (how similar to an sphere are the nuclei) are detected (fig. 3D, right panel). In contrast, progenitor cells exhibit a higher standard deviation in nuclei shape compared to differentiated cells. This is consistent with previous studies correlating nuclei shape with cell movement [8] (given that progenitors undergo interkinetic nuclear migration [9], their nuclei are expected to be elongated compared to those of differentiated cells).

Quantitative values of the total number of progenitors (P, orange dots) and differentiated cells (D, green dots) are depicted in Fig. 3D. Based on our data and previous studies [7], cells with $V_j^{Sox2} \approx V_j^{GFP}$ IP are still cycling, are thus counted as progenitors for the purpose of this study. Optimal fitting for P cells is a sigmoidal function (orange line, best fit determined using the Akaike information criterion as explained in Supplementary Information), while the dynamics of D cells aligns well with a power law (green line). The ribbons in the fitting represent the 95% confidence interval of the fitting, obtained using the Delta Method (details in Supplementary Information).

Next, the fitted values for P and D are used as input for a set of analytical equations based on a branching process formalism developed by our group [10]. In essence, equations 1-2 provide values for the difference between rates of proliferative and differentiative symmetric divisions ($pp - dd$), as well as the average cell cycle length (T) of cycling cells, with temporal resolution and higher accuracy compared to BrdU or EdU-based methods [11].

The growth fraction γ (estimated as the ratio of Sox2+ cells that are also positive for Pcna immunostaining) decreases from $\gamma = 1.0$ at 20 hpf to $\gamma = 0.85$ at 35 hpf, before rising again to $\gamma = 0.95$ at 48 hpf. The rate of apoptosis $\emptyset$ (estimated by quantify cells positive for staining against the active form of Caspase 3, a key mediator of apoptosis) is less than 0.1% during this first 48 hours, in agreement with previous studies [12, 13]. Based on this, we can safely discard apoptosis from our analysis ($\emptyset = 0$).

Using the values for $\emptyset$ and γ, along the fitted values for $\mathbf{P}$ and $\mathbf{D}$, the calculation for the average mode of division $pp - dd$ (Fig. 3F blue line, left vertical axis) suggests a shift from predominately symmetric proliferative divisions ($pp - dd \approx 1$ at 20 hpf) to increased differentiation of RPCs ($pp - dd \gtrsim 0.35$ at 48 hpf). Concurrently, the average cell cycle T (Fig. 3F yellow line, right vertical axis) accelerates from $T \gtrsim 12$ hours at 20 hpf to $T \gtrsim 6$ hours at 48 hpf.

In conclusion, the quantitative data provided by our framework enables us to assess the balance between cycling progenitors and terminally differentiated cells during the initial wave of neurogenesis in the zebrafish retina, providing also the measurement of key morphological features at tissue and single cell level. The values obtained for progenitors and differentiated cells, when utilized as input for the branching equations, suggest that the increase in differentiation is concurrent with a decrease in the length of the cell cycle.
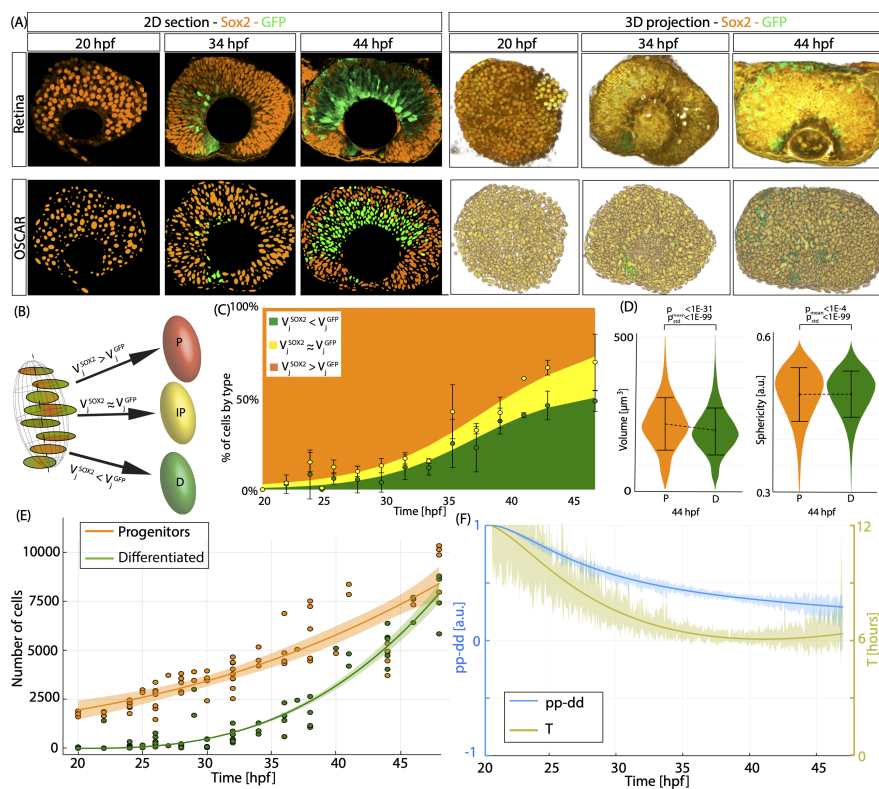
Figure 3: **Quantification of the dynamics of proliferation and differentiation of the zebrafish retina**. (A) Representative sections and 3D-view of tissues stained with Sox2 (orange) and GFP (green) at different developmental stages. Below each image, we plot the corresponding digital representation to illustrate the output of OSCAR. (B) Scheme of the decision process to establish identity of the 3D-Objects detected by OSCAR. (C) Percentage of cells in the retina where Sox2 staining intensity is measured as higher (orange), lower (green) or similar (yellow) that GFP immunostaining. (D) Quantification of differences in size and sphericity between nuclei of progenitors and differentiated cells for a single image at 44 hpf (mean and standard deviation are illustrated on top of the violin plot). (D) Quantification of the number of progenitors (orange dots) and differentiated cells (green dots) overtime for 60 data points. Parameters for sigmoidal fitting (orange line) $P(t) = 2E3 + 265 \cdot t$. Differentiated cells (green line) are fitted as, $D(t) = t^{2.75}$. Ribbons illustrate the 95% confidence interval of the fitting. (E) Average T (yellow, right vertical axis) and $pp - dd$ (blue, left vertical axis) obtained from equations [1, 2], when using as input the fitted curves $P(t)$ and $D(t)$. Ribbons illustrate the 95% confidence interval, calculated using the Delta Method (See Supplementary Information).

9

3. Hh signaling promotes cell cycle exit and cell cycle progression in the developing vertebrate retina.

One of the most well-characterized regulators of developmental processes is the Hedgehog (Hh) signaling pathway, involved in the genesis of nearly all organs in mammals. Additionally, in adult tissues, it governs homeostasis and regeneration, and its dysregulation is associated with various types of cancer [14]. One of the most extensively studied roles of Hh is as a major driver of patterning and differentiation of neural progenitors during embryogenesis [15, 16].

In the developing vertebrate retina, Hh is involved in a positive feedback loop that generates a traveling front [17] of Hh expression that starts at the the ventro-nasal region and spreads centrifugally to organize the neurogenesis across the epithelial sheet [18, 19, 20], similarly to the propagating wave of differentiation across the eye primordium in Drosophila [21, 22, 23, 24].

To characterize the specific role of Hh in regulating both the mode and rate of division during retinal development, zebrafish embryos from the Tg(Atoh7:GFP) line are cultured in the presence of Cyclopamine [25], a small molecule inhibitor that selectively binds to the Hh receptor Patched and interrupts Hh pathway activity (see Methods). These embryos are then processed, imaged, and quantified as in previous sections. Figure 4A displays a representative section of a zebrafish retina at 39 hpf from both a control embryo (left) and a +cyclopamine treated embryo (right), stained with Sox2 (orange) and anti-GFP (green). Comparison of these sections suggests that cyclopamine-treated retinas exhibit a similar size but a smaller proportion of GFP+ cells. However, this difference could also stem from variability between embryos or sections of the same retina, as the proportions of progenitors and differentiated cells are highly dependent on the section. To determine the statistical significance of these differences, we quantified approximately 50 embryos at different hpf (Figure 4B, solid line), revealing a trend that aligns well with an exponential curve, with a negligible reduction in size compared to the control conditions (dashed line).

Conversely, we observe a statistically significant increase in the numbers of progenitors (fig. 4C, orange dots, orange solid line) and a reduction in differentiated cells (fig. 4C, green dots, green solid line) compared to the control (dashed lines, reproduced here to facilitate comparison), particularly at later time points.

To determine whether this shift results from variations in the mode and/or rate of division, these numbers are utilized as input in equations 1-2 (cell death and quiescence remain equivalent between control and +cyclopamine conditions). The output for the mode of division (fig. 4D, blue solid line, left vertical axis) shows a gradual shift towards more proliferative divisions, compared to the control (dashed blue line). Interestingly, this increase in the rate of proliferative divisions is expected to generate more progenitors, leading to larger retinas (as more cycling cells would produce more progeny). However, this expectation contradicts both prior studies [26] and with our own findings (fig. 4B). This discrepancy is clarified when we focus on the cell cycle length of progenitors (fig.
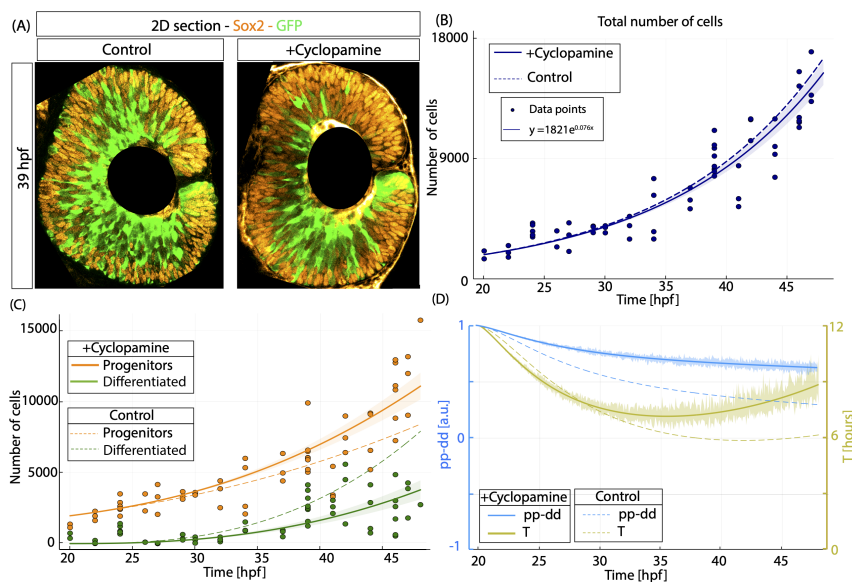
10

Figure 4: **Hh promotes differentiation and cell cycle progression in the developing vertebrate retina**. (A) Representative sections of tissues stained with Sox2 (orange) and GFP (green) at 39 hpf for control and +cyclopamine treated embryos. (B) Total number of cells for 50 +cyclopamine treated embryos fixed at different hpf. Solid line corresponds to exponential fitting. Ribbons correspond to 95% confidence of fitting. Fitting for control conditions (dashed line), is added for comparison. (C) Number of progenitors (orange dots) and differentiated cells (green dots) overtime of +cyclopamine treated embryos. Solid lines correspond to the fitting for progenitors and differentiated cells. Ribbons correspond to 95% confidence of fitting. Fitting for control conditions is added (dashed lines) for comparison. (D) Average T (yellow, right vertical axis) and $pp - dd$ (blue, left vertical axis) obtained from equations 1-2, when using as input the fitted curves $P(t)$ and $D(t)$. Ribbons illustrate the 95% confidence interval of the fitting, calculated using the Delta approximation (see Supplementary Information).

4D, yellow solid line), that is now in average slower than the control (yellow dashed line). We hipothesize that the balance between an increased number of progenitors and a slower cell cycle is the underlying reason for the unchanged overall size of the retina.

In conclusion, our analysis shows that cyclopamine treatment in developing zebrafish retinas diminishes differentiation by fostering more proliferative divisions and decelerating the cell cycle, consistent with a role of Hh in regulating neurogenesis by promoting the cell cycle exit, but also cell cycle progression.

4. Wnt signaling promotes cell cycle progression during the development of the vertebrate retina.

The Wnt signaling pathway plays a pivotal role in various biological processes including tissue patterning, regeneration, cell survival, stem cell regulation, cell-

to-cell interactions, cell cycle control, proliferation, self-renewal, and cell-fate decisions [27, 28]. Dysregulation of Wnt signaling is implicated in human degenerative diseases and cancer, making it an attractive target for pharmaceutical interventions and therapeutics. Specifically, in the context of the developing vertebrate retina, disruptions in Wnt signaling have been associated with retinal disorders such as retinitis pigmentosa, familial exudative vitroretinopathy, and Norrie's disease [29].

The role of Wnt in the vertebrate retina seems to be highly context dependent, ranging from regulating retinal field establishment and specification in early embryos, to maintaining retinal stem cell identity during neurogenesis and regeneration in adult animals [30, 29, 31]. In the early stages of retinal development, Wnt signaling has been linked to cell cycle progression, proliferation, apoptosis, and differentiation in Medaka [32]. Notably, both the canonical (via β-catenin) and the non-canonical (not involving β-catenin) pathways of Wnt signaling have been implicated in stem cell maintenance and specification of the neural retina [33, 34].

To characterize the specific role of the canonical Wnt signaling in the development of the neural retina, we cultured embryos in the presence of XAV939, a potent small molecule inhibitor known to increased the degradation of β-catenin [35]. The results, summarized in fig. 5, depict two mid sections of control and XAV939 treated retinas at 39 hpf in fig. 5A. Upon visual comparison, a reduction in cells expressing Atoh7+ cells (EGFP) is observed, alongside a decrease in overall size. Quantification of the number of total cells in 30+ retinas in 3D (fig. 5B) reveals that indeed, the number of cells in embryos growing in the presence of XAV939 (solid line) over time follows an exponential function that increases more slowly than in control conditions (dashed line). Comparison of the changes in number of progenitors and differentiated cells over time (fig. 5C) indicates a dynamics similar to control conditions, with reductions observed in both the numbes of progenitors and differentiated cells.

Finally, to quantify whether these differences are attributable to changes in the cell cycle and/or the mode of division, we input the numbers of P and D cells into the branching equations (values for quiescence and apoptosis remains similar to that of control conditions). The output of the equations (fig. 5D) reveals a similar value of mode of division than in the control (solid and dashed blue lines, respectively), but a significantly longer cell cycle (solid yellow line, compared to the dashed yellow line). In conclusion, our results suggest that, despite the multiple potential roles reported for Wnt signaling [27, 28, 32], canonical Wnt signaling in the developing vertebrate retina primarily promotes cell cycle progression of RPCs, with minimal effect on their differentiation.

5. Notch-Delta reduces the proliferation rate of RPCs in the developing vertebrate retina.

Notch is a highly conserved local cell signaling mechanism involved in the regulation of developmental processes, tissue homeostasis, regeneration, stem cell differentiation, proliferation, apoptosis, adhesion, epithelial-mesenchymal
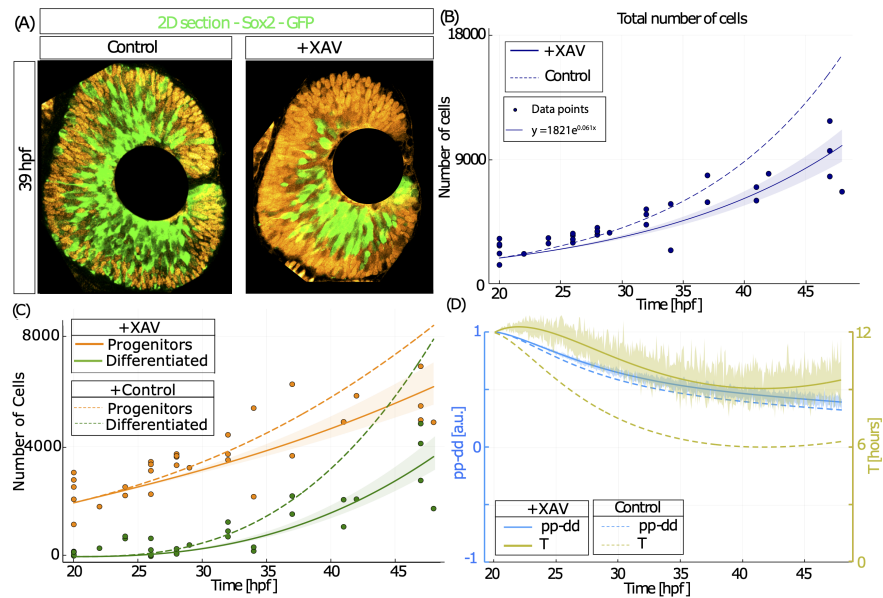
Figure 5: **Wnt promotes cell cycle progression of retinal progenitors**. (A) Representative sections of tissues stained with Sox2 (orange) and GFP (green) at 39 hpf for control and +XAV939 treated embryos. (B) Total number of cells for 50 +XAV939 treated embryos fixed at different hpf. Solid line corresponds to exponential fitting. Ribbons correspond to 95% confidence of fitting. Fitting of control conditions (dashed line), is added for comparison. (C) Number of progenitors (orange dots) and differentiated cells (green dots) overtime of +XAV939 treated embryos. Solid lines correspond to fitting of progenitors and differentiated cells. Ribbons correspond to 95% confidence of fitting. Fitting of control conditions is added (dashed lines) for comparison. (D) Average T (yellow, right vertical axis) and $pp - dd$ (blue, left vertical axis) obtained from equations 1-2, when using as input the fitted curves $P(t)$ and $D(t)$. Ribbons illustrate the 95% confidence interval of the fitting, calculated using the Delta approximation (see Supplementary Information).

transition, migration, angiogenesis, and cell-cell communication. It acts via the interaction of specific ligands with the Notch transmembrane receptor, which triggers the release of its intracellular domain that then enters the nucleus and drives the expression of target genes [36, 37].

In the context of the developing vertebrate retina, Notch1 is Notch1 expression is typically associated with proliferating progenitors and is implicated in maintaining RPCs while inhibiting cell differentiation [38]. Interestingly, other studies suggest that Notch1 actually triggers differentiation [7, 39, 40, 41, 42, 43], proposing that variables such as timing, duration, and intensity of signaling determine whether it promotes or inhibits differentiation [37, 44]. Regarding the cell cycle, Notch signaling has been demonstrated to facilitate cell cycle progression by upregulating cyclins and other cell cycle-promoting factors [45], although it has also been shown to reduce the proliferation rate in other contexts [46, 47].

To assess the specific role of Notch in the mode and rate of division in the developing retina of zebrafish, we cultured embryos in the presence of DAPT [48], a potent and highly specific small molecule inhibitor that blocks Notch signaling. Visual comparison of treated embryos fixed at 48 hpf (fig. 6A) reveals increased structural organization compared to the control (resembling control embryos older than 48 hpf). Quantification of the total number of cells for around 40 full 3D retinas at different hpf (fig. 6B, solid line) fits an exponential growth that is slightly faster than in the control (dashed line). The number of progenitors and differentiated cells (fig. 6C) reveals an significant increase in the number of differentiated cells (green solid line) and a slight decrease in the number of progenitors (orange solid line), compared to the control (dashed lines).

To determine whether these changes correspond to alterations in the mode and/or rate of division, we input these values into the branching equations, and the resulting data is plotted in fig. 6D. Interestingly, the rate of differentiation $(pp - dd)$ (blue solid line) appears to be similar to that of control conditions (dashed blue line), while the cell cycle length (T) is shorter (yellow solid line) compared to the control (dashed yellow line). In conclusion, based on the observed effects following pathway inhibition, our analysis indicates that Notch signaling in the developing vertebrate retina reduces the proliferation rate of RPCs but does not affect the differentiation rate.

6. FGF signaling promotes cell cycle exit and cell cycle progression in the developing vertebrate retina.

As with other major signaling pathways, Fibroblast Growth Factor signaling (FGF) plays diverse roles in early embryogenesis, from inducing the patterning of embryonic axes to the induction and/or maintenance of various cell lineages and the coordination of morphogenetic movements [49]. During organogenesis, FGF activity has been associated with the maintenance and promotion of growth, differentiation, survival, and patterning of progenitor cells [36]. In the context of the developing vertebrate retina, it has been suggested that FGF initiates the nasotemporal patterning of the zebrafish retina [50], and that an FGF
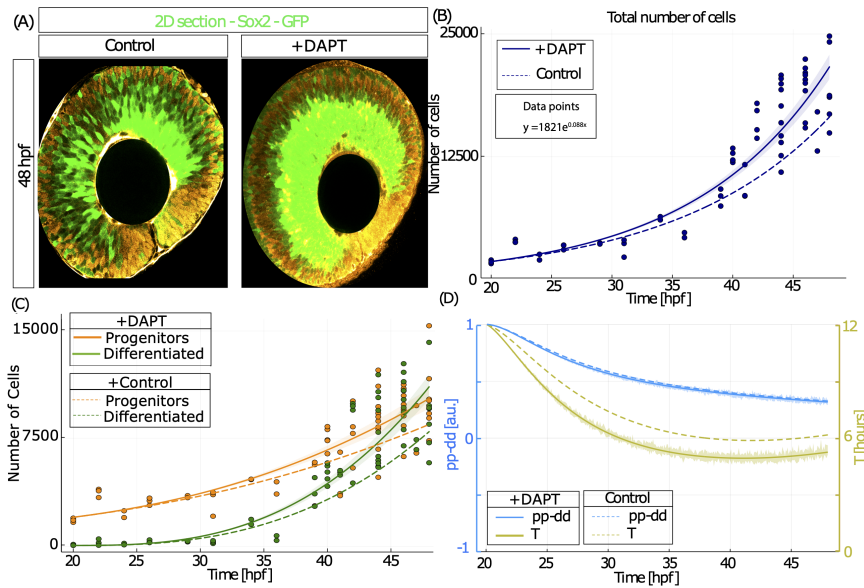
Figure 6: **Notch signaling reduces the proliferation rate of RPCs**. (A) Representative sections of tissues stained with Sox2 (orange) and GFP (green) at 48 hpf for control and +DAPT treated embryos. (B) Total number of cells for 40 +DAPT treated embryos fixed at different hpf. Solid line corresponds to exponential fitting. Ribbons correspond to 95% confidence of fitting. Fitting of control conditions (dashed line), is added for comparison. (C) Number of progenitors (orange dots) and differentiated cells (green dots) overtime of +DAPT treated embryos. Solid lines correspond to fitting of progenitors and differentiated cells. Ribbons correspond to 95% confidence of fitting. Fitting of control conditions is added (dashed lines) for comparison. (D) Average T (yellow, right vertical axis) and $pp - dd$ (blue, left vertical axis) obtained from equations 1-2, when using as input the fitted curves $P(t)$ and $D(t)$. Ribbons illustrate the 95% confidence interval of the fitting, calculated using the Delta approximation (see Supplementary Information).

signaling center coordinates the differentiation of RPCs, serving as a necessary and sufficient mediator of midline signals [51]. Regarding the cell cycle, FGF1 overexpression has been shown to inhibit cell cycle arrest [52], while reducing FGF15 decreases or delays the expression of transcription factors that regulate the cell cycle [53]. However, in the context of neurogenesis, the role of FGF is less clear, as inhibition of FGF increases the levels of cyclin D1 but decreases the levels of cyclin D2 [54].

To assess the specific role of FGF signaling in the developing retina, we cultured embryos treated with SU5402, a protein tyrosine kinase inhibitor that blocks autophosphorylation of receptors including FGFR1. Following the same protocol as in previous cases (see Methods), we summarized the results of over 30 full 3D retinas in fig. 7. SU5402-treated retinas appear smaller and less mature than control retinas at 48 hpf (fig. 7A). Regarding cell numbers (fig. 7B), FGF inhibition (solid line) affects the overall size, reducing the speed of the exponential growth (compared to the fitting of control conditions, dashed line). Results separated for progenitors (orange) and differentiated cells (green) are shown in fig. 7C. The solid lines represent the fitting of the experimental values (compared to the dashed lines for control conditions), indicating that the overall reduction in size is primarily due to a significant reduction in differentiation, with minimal change in the number of progenitors.

The direct effect in the mode and rate of division becomes apparent when the number of P and D are used as input to the branching equations. Our data (fig. 7D) clearly indicates a reduction in differentiation (blue solid line), along with a notable increase in the average cell cycle length of progenitors (yellow solid line) compared to the control (blue and yellow dashed lines, respectively). This combination of effects elucidates the observed reduction in size: while an increase in proliferative divisions alone should lead to larger retinas, the slower cell cycle counteracts this, resulting in retinas with less differentiation that are also smaller. Based on this data, our results suggest that FGF signaling promotes both differentiation and cell cycle progression, similarly to Hh.

7. Discussion

This study presents a novel framework designed to characterize the dynamics of proliferation and differentiation in developing tissues across the four dimensions (3D + time), specifically tailored for images acquired *in toto*. When applied to the developing zebrafish retina, the framework provides us with the numbers of progenitors and terminally differentiated cells at different time points, that serve as input for equations that quantify the average mode and rate of division with temporal resolution. Finally, by comparing these values following chemical inhibition, we can elucidate the effects of key signaling pathways on the regulation of the balance between proliferation and differentiation during the initial wave of neurogenesis.

Our findings indicate that total cell numbers are approximately 10% lower than those reported in previous studies based on 2D slices [55] or 3D images [12]. Moreover, our findings confirm that the volume of the retina doubles between
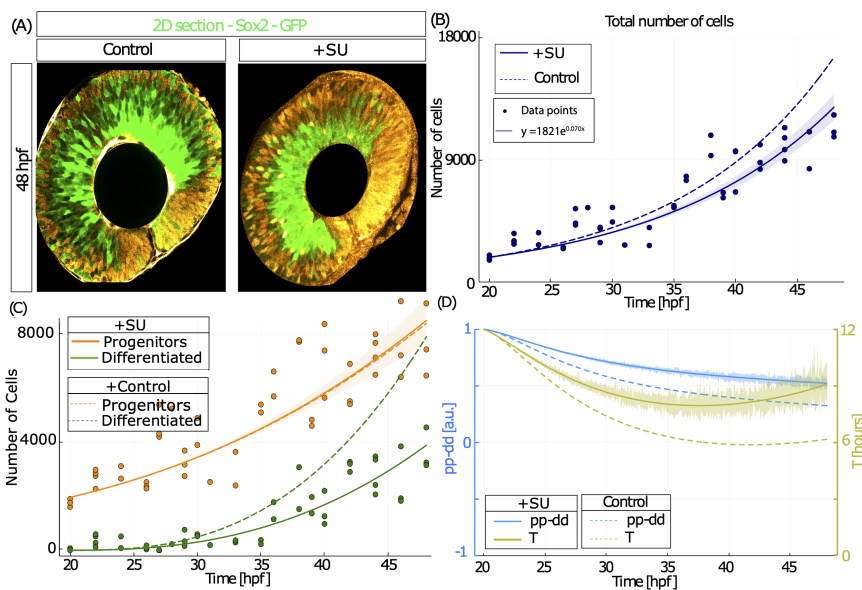
16

Figure 7: **Fibrobrast Growth Factor signaling promotes differentiation and cell cycle progression**. (A) Representative sections of tissues stained with Sox2 (orange) and GFP (green) at 48 hpf for control and +SU5402 treated embryos. (B) Total number of cells for 50 +SU5402 treated embryos fixed at different hpf. Solid line corresponds to exponential fitting. Ribbons correspond to 95% confidence of fitting. Fitting of control conditions (dashed line), is added for comparison. (C) Number of progenitors (orange dots) and differentiated cells (green dots) overtime of +SU5402 treated embryos. Solid lines correspond to fitting of progenitors and Differentiated cells. Ribbons correspond to 95% confidence of fitting. Fitting of control conditions is added (dashed lines) for comparison. (D) Average T (yellow, right vertical axis) and $pp - dd$ (blue, left vertical axis) obtained from equations 1-2, when using as input the fitted curves $P(t)$ and $D(t)$. Ribbons illustrate the 95% confidence interval of the fitting, calculated using the Delta approximation (see Supplementary Information).

20 hpf and 32 hpf (consistent with prior studies [12]). However, we observe a linear growth in volume (Fig. 2C), rather than the exponential growth pattern previously described [12]. We propose that this difference may be attributed to the reduced temporal resolution in previous studies (6 hours between time points), in contrast to the 2-3 hour intervals between our data points.

Our analysis also indicates an increase in cell density during this early phase of neurogenesis, potentially affecting both proliferation and differentiation processes. Previous research suggests that cell density is pivotal in regulating neural precursor cell function, influencing the expression levels of various proteins and reactive oxygen species (ROS) [56]. Additionally, cell density is directly associated with resistance to oxidative stress [57], as well as cell differentiation, survival, migration, and proliferation [58, 59].

Regarding the cell cycle, our results are in line with previous research indicating average cell cycle values of around 8 hours from 24 to 28 hpf [55], as well as single-cell values ranging from 4 to 11 hours [60]. Moreover, prior studies have shown that the majority of cells incorporated BrdU at 22 hpf [55], which is consistent with our estimation of the growth fraction using Pcna immunostaining at early time points.

In terms of the balance between proliferation and differentiation, recent studies have focused on the dynamics of differentiation waves [61, 5] and the subsequent translocation of cells post-differentiation [62]. Interestingly, our results indicate that division events produce more progenitors than differentiated cells ($pp - dd > 0$) across all time points tested. However, this observation appears contradictory to the eventual dominance of differentiated cells over progenitors by the end of our observation period. This apparent discrepancy can be explained by noting that differentiated neurons accumulate over time, while progenitors continue to cycle.

The functions of the Hh, Wnt, Notch, and FGF signaling pathways have thoroughly investigated previously. Nonetheless, it is not uncommon to come across studies suggesting a specific role for for one signal while others advocate for the complete opposite [63, 64]. Here, we outline our observations following chemical inhibition of Hh, Wnt, Notch, and FGF signaling pathways concerning the balance between proliferation and differentiation, and their alignment with previous studies:

Hh - Our studies indicate that Hh plays a dual role in promoting both cell cycle exit and cell cycle progression. This finding aligns with the established roles of the Hh pathway in promoting the cell cycle exit of RPCs [20]. Typically, a simple reduction in differentiation following Hh inhibition would lead to an increase in cycling progenitors, potentially resulting in larger final retinas (an outcome inconsistent with previous observations [26] and our own data). However, our results demonstrate that the size is maintained due to a simultaneous increase in the cell cycle length, suggesting a role for Hh in promoting cell cycle progression, consistent with observations in other systems, such as the Drosophila compound eye [65], chick neural tube [54, 66, 67, 68], and mouse neocortex [69].

This scenario aligns with the role of Hh in transitioning cells from a slow-

cycling progenitor to a faster-cycling progenitor more ready to terminally differentiate. An alternative possibility is that Hh promotes cell cycle exit and differentiation in cells at more central regions (where differentiation is taking place) while accelerating the cell cycle in more peripheral regions of the tissue, where cells are slated to differentiate later in time. This scenario could be best explored in time-lapse experiments, which will be the focus of our future work.

Wnt - Our studies indicate that the primary role of Wnt is to promote cell cycle progression, aligning with previous studies in cell culture where Wnt signaling induces cyclin D1 expression via ErbB1, promoting the transition from G1 to S phase [70, 71], and represses the cell cycle inhibitor p27 [72]. However, our results show no indicate no discernible change on the balance between proliferative and differentiative divisions following Wnt inhibition, contrary to other studies that link Wnt signaling with differentiation [33, 34, 32].

Notch-Delta - Our data indicate that Notch influences the dynamics of morphogenesis by slowing down the cell cycle. This finding contradicts previous studies associating Notch with the promotion of cell cycle [45, 73, 74, 75]. Conversely, Notch is known to restrict Wnt signaling in a Notch-ON/Wnt-OFF state [76]. When this is considered in conjunction with our earlies finding of Wnt's role in promoting the cell cycle in the developing vertebrate retina, inhibition of Notch should result in a faster cell cycle, aligning perfectly with our observations.

In terms of differentiation, Notch inhibition results in a more pronounced increase in the differentiated population compared to the progenitors (fig. 6A). This observation may suggest that Notch promotes progenitor self-renewal, a conclusion proposed in previous studies [38]). Interestingly, the branching equations demonstrate that this rise in the proportion of differentiated cells does not involve a change in the mode of division (fig. 6C). To explain this paradox, we must consider that differentiated cells accumulate over time, while progenitor cells continue cycling and generating new cells. Consequently, an acceleration of the cell cycle leads to increased accumulation of differentiated cells, creating the false impression that the mode of division has changed.

FGF - Our studies indicate that FGF promotes both differentiation and cell cycle progression, consistent with previous studies that show reduced Atoh7 expression following inhibition of FGF signaling. This is also consistent with reports of the cooperative role of Fgf3/Fgf8 in initiating neuronal differentiation in the retina, serving as an inductive signal originating from the optic stalk to trigger retinal differentiation [51]. A similar role for FGF has been proposed in the development of the ear placode [77]. Considering the numerous experimental pieces of evidence supporting direct cross-talk between Hh and FGF, it is reasonable to expect that inhibition of FGF and Hh would have similar effects on the mode and rate of division.

Interplay between mode and rate of division - Focusing on the connection between the mode of division and the duration of the cell cycle, our findings reveal a consistent pattern where the cell cycle always accelerates as differentiation increases. This link holds true under both control (fig. 3) and experimental conditions (where Hh and FGF inhibition reduce both differentia-

tion and cell cycle progression, as shown in fig. 4 and fig. 7). This observation may indicate that differentiative divisions have a shorter cell cycle on average, in agreement with studies reporting an acceleration of the cell cycle during the onset of differentiation in Xenopus [78]. Moreover, our research indicates that changes in the mode of division are correlated to changes in the cell cycle, but that the cell cycle can be modulated independently of the mode of division (as seen with Wnt and Notch inhibition, as illustrated in fig. 5 and fig. 6).

8. Conclusions

In this contribution, we present a novel experimental/computational/theoretical framework specifically designed to explore the developmental dynamics of three-dimensional tissues, optimized for analyzing images with low resolution and signal-to-noise ratio typical of experiments conducted *in toto* and/or *in vivo*. Applied to the developing vertebrate retina, the framework enables us to examine various key aspects of the initial wave of differentiation, including growth, density, composition, and the average mode and rate of division with temporal resolution. By comparing changes in these parameters following small molecule inhibition, we observed that Hh and FGF activity play similar roles in promoting differentiation and cell cycle progression, while Wnt and Notch primarily increase and decrease the rate of division, respectively. The accuracy, simplicity, and direct applicability of the framework strongly facilitate its direct application to studying the development of other three-dimensional tissues and organs with quantitative precision.

9. Methods and Materials

9.1. Animals and Experimental procedure with zebrafish embryos

Experiments are conducted using embryos from the Tg(atoh7:GFP) zebrafish line, which has been genetically engineered to express GFP as a marker for Atoh7 expression [6]. Atoh7 is a member of the basic helix-loop-helix (bHLH) proneural transcription factor family, expressed in terminally differentiating and differentiated cells and plays a crucial role in regulating neurogenesis in the retina [79, 80]. The animals are maintained and bred according to established protocols [81]: (1) Adult zebrafish are maintained at 28°C in specialized cuvettes in the fish facility with all permits and constant supervision. To obtain fertilized eggs, adults are placed in mating cuvettes overnight with males and females separated. (2) The barrier is removed the following morning, and the presence of eggs is checked every 20 minutes to accurately determine the date of birth based on visual inspection [82]. (3) Fertilized eggs are collected and cultured in fresh E3 medium 1X (5 mM NaCl, 0.17 mM KCl, 0.33 mM CaCl2, 0.33 mM MgSO4, Methylene Blue), supplemented with phenylthiourea (PTU) at 0.003% from 20 hours post-fertilization (hpf) to prevent pigmentation, with media replacement every 24 hours. (4) Sets of 20 embryos at similar hpf are transferred to p100 Petri dishes and placed in an incubator at 28°C. (5) Pronase (Merck,

CAS-No 9036-06-0) at a concentration of 1:100 in E3 1x medium is added at 20 hpf to remove the chorion [83]. (6) Subsequently, embryos are divided into sets of 5 in 6-multiwell plates, and either DMSO (control) or the corresponding small molecule inhibitors (Supplementary Table 2) are added. (7) Embryos are collected at developmental stages between 24 and 48 hpf and fixed overnight at 4°C in a 10% Formalin solution (Sigma, HT501128). (8) Subsequently, embryos undergo dehydration using series of methanol dilutions (0%, 25%, 50%, 75%, and 100%) and then stored at -20°C for a minimum of overnight and a maximum of six months, (protocol adapted from ref. [84]).

9.2. in toto immunostaining

(1) Re-hydration of embryos is conducted using the previous serial dilutions of methanol, but in reverse order. (2) All subsequent solutions are prepared in PBS 1X with 0.6% triton to enhance permeability of antibodies and dyes. (3) Embryos undergo incubation in proteinase K (10 ug/ml) for a specified duration (refer to Supplementary Table 1) to facilitate penetration of antibodies and dyes. (4) The reaction is halted by brief exposure to 10% Formalin (Sigma, HT501128) for 20 minutes at room temperature. (5) Embryos are washed three times with PBS 1X and 0.6% triton. (6) Subsequently, embryos are incubated in a blocking solution (10% FBS in PBS 1X and 0.6% triton) overnight at 4°C to prevent non-specific antibody binding. (7) Embryos are incubated with the corresponding primary antibodies, diluted in a solution of 2% FBS in PBT 0.6%, overnight at 4°C. (8) The primary antibody solution is washed three times for five minutes each. (9) Embryos are then incubated in a solution of 2% FBS in PBT 0.6% with secondary antibodies and nuclei staining for 1 hour at room temperature. (10) Finally, embryos undergo three washes with PBT 0.6% followed by PBS.

The primary antibodies used are: chicken anti-GFP (1:1000, Abcam ab137827), rabbit anti-Sox2 (1:1000, GeneTex GTX124477), mouse anti-Pcna (1:100; Invitrogen, MA5-11358) and rabbit anti-PH3 (1:250; Merck-Millipore, 06-570). The secondary antibodies used are: goat anti-Chicken-488 (1:500; ThermoFisher, A-11039), goat anti-mouse-55 (1:500; ThermoFisher, A-21157) and donkey anti-rabbit-555 (1:500; ThermoFisher A-31573). DNA is stained with the interkalant nuclear agent 647 nm fluorophore To-Pro3 (1:500; ThermoFisher, T-3605) for all samples.

As a positive control for Active Caspase 3 immunostaining, we present in Supplementary Figure 4 a zebrafish retina at 52 hpf (when apoptosis becomes non-negligible) stained against Active Caspase 3 [85].

9.3. Sample mounting, image acquisition and processing

Samples are mounted in homemade chambers with glass slides using 25-50 μL of RapiClear© 1.49 (SunJin Lab). Confocal images are captured using a Leica SM800 confocal microscope, with a thickness of 1 μm determined by the pinhole settings. An overlapping of 0.2 μm between confocal sections is established to ensure proper 3D reconstruction. The resolution in the confocal plane is 325x325 μm, while the resolution in the Z direction is determined by the number of confocal sections (ranging from 64 to 120 μm).

Image processing is conducted using Julia [86] scripts and packages, and FIJI macros [87]. Isolation of the neural retina in the image is achieved using a custom macro designed to define the bounding boxes of the region of interest in the XY and XZ planes in To-Pro3 nuclear staining images. The lens is extracted by approximating it to an ellipsoid using the $3DDrawShape$ plugin [88]. Further details regarding specific filtering and image processing for each channel can be found in the Supplementary Information.

9.4. Object Statistical Clustering of Adjacent Regions (OSCAR)

Automated analysis of densely packed 3D biological images is affected by sample thickness. Objects near the tissue surface are clear and well defined, but resolution and signal-to-background ratio diminish as we focus deep into the tissue decreases deeper into the tissue, due mainly to increase scattered photons caused by light passing through thick biological samples, and reduced dye permeability into the deepest regions of the tissue .

With these limitations in mind, we have developed OSCAR (Object Statistical Clustering of Adjacent Regions), which comprises a set of algorithms and statistical tools designed to cluster sections of an object into three-dimensional objects. OSCAR has been specifically tailored to perform effectively in realistic biological three-dimensional images, using an efficient and robust algorithm to establish interactions between objects in consecutive planes (further elaborated in the Supplementary Information). The primary innovations of OSCAR are summarized as follows:

- Improved performance: OSCAR in written in Julia Language, a modern fast language optimized for mathematical and statistical analysis. In addition, OSCAR uses fitted parameters for the clustering, resulting in much faster computations and allowing us to perform multiple statistical filtering.

- Ease of use: OSCAR does not require parameter adjustments or neural network training, making it accessible to users with no experience in image processing or programming skills.

- Efficient Storage: OSCAR conducts calculations through nonlinear fitting to parametric functions rather than bounding boxes, leading to more efficient data storage and processing, enabling its utilization on conventional personal computers.

- Designed for realistic images: OSCAR overcomes under-segmentation and over-segmentation errors inherent in images with high object density and low signal-to-background ratios by leveraging 3D information (clustering a new plane into a given three-dimensional object depends on the features and properties of the previous planes of this particular three-dimensional).

- Broad Applicability: OSCAR has been tested to function effectively across a variety of images, including artificial images, cardiac micro-tissues, neurospheres, human brain biopsies, and numan retinal organoids.

- Classification and Sorting with Spatial Resolution: OSCAR can categorize cells into different groups based on specific biological markers. In this sense, OSCAR functions akin to a flow cytometer while also offering spatial information.

- Compatibility: OSCAR is designed as a central pipeline compatible with deep-learning algorithms and other object separation algorithms.

Code generated and used as part of the present manuscript available in the following link: https://github.com/davidgmiguez/OSCAR.

9.5. Generation of output figure

The 3D digital reconstructions generated from OSCAR's output are generated using "3D Viewer" and "3D Draw Shape", within the 3D ImageJ Suite package in FIJI [89, 88]. In this study, each object detected is depicted as an ellipsoid positioned at its centroid, with orientation and dimensions determined by its x-length, y-length, and z-length. Objects in the output image are color-coded based on cell identity, determined through immunostaining processing. The Lookup Table (LUT) for each image is adjusted accordingly, with the color legend provided in each figure for reference.

Branching Process tool

Average cell cycle length and mode of division are measured based on the following equations developed by our lab [10] using a branching process formalism:

$$pp - dd = \frac{\phi \Delta D + \gamma \Delta P}{\gamma (\Delta D + \Delta P)} \tag{1}$$

$$T = t \cdot \frac{\log(1 - \phi + \gamma(pp - dd))}{\log \frac{P(t)}{P_0}} \tag{2}$$

Input values are: $\Delta P = P_t - P_0$ and $\Delta D = D_t - D_0$ represent the number of progenitors and differentiated cells generated in a given window of time $\Delta t = t - t_0$; $\emptyset$ corresponds to the rate of cell death of the progenitors and γ is the growth fraction (rate of progenitors that are actively cycling). $\emptyset$ has been estimated using Active Caspase 3 immunostaining (Supplementary Figure 4). γ has been estimated using Pcna immunostaining (Supplementary Figure 3). One of the main advantages of Pcna over BrdU analogs to estimate the growth fraction is that it does not require cumulative curve estimation or previous manipulation of the embryos (it is well known that thymidine analogs affect cell cycle progression [11]). On the other hand, Pcna is down-regulated during M-phase so, this needs to be taken into account to establish the growth fraction using this method (see Supplementary Information).

Output value $pp - dd$ can be identified with a measure of the differentiation dynamics (pp and dd are the rate of symmetric proliferative and differentiative

23

divisions, respectively), and goes from 1 (all divisions being symmetric proliferative) to -1 (all divisions being symmetric differentiative). In this general form, the model does to distinguish if cells generate from asymmetric pd or symmetric (pp or dd) divisions (these two scenarios are mathematically equivalent).

Nonlinear Fitting, Error Propagation and Statistical Analysis

To facilitate visualization of dynamics and differences between control and experimental conditions, data are accompanied by fitted curves. The best fitting estimation for each condition in control experiments is determined using Akaike's Information Criterion [90] (see Supplementary Information). Fitting of experimental conditions is conducted with consideration for mild inhibition levels resulting in gradual changes in dynamics. Moreover, since inhibitors are introduced at t=20 hpf, values at this time point are equivalent between control and experimental conditions. Thus, the dynamics in experimental conditions are fitted with a single parameter that modulates the control fitting. This approach yields curves for both control and experimental conditions that align at 20 hpf and gradually diverge as the drug's effects manifest over time.

These curves, along with the confidence intervals for the fitting, serve as input for the branching equations 1-2. However, due to their nonlinear nature, estimating uncertainty in T and $pp - dd$ cannot be achieved through simple error propagation of the uncertainties obtained from the fitted P and D curves. Consequently, a combination of the Delta method [91] and Monte Carlo simulation [92] is employed to assess how uncertainty in P and D propagates into the uncertainty in the calculation of $pp - dd$ and T (detailed explanation provided in Supplementary Information).

To assess the statistical significance of the fitting for the total number of cells and number of differentiated cells, we perform a z-test for the coefficients of the regression between control and experimental conditions. Results are listed in Supplementary Table 3. This test is not suitable for comparing different functional forms (as in numbers of progenitor cells). In this case, we use the Root Mean Squared Errors (RMSE) of the second half of the regressions to compare the goodness-of-fit using the fitting for the control (RMSE*) and the same fitting modulated with an extra parameter (RMSE). Results listed in Supplementary Table 4 show that the modulation improves the RMSE of the fitting.

10. Acknowledgments

11. Author contributions

MLT, DPD and DGM designed research. MLT and DPD performed research. MLT, DPD, DMD and DGM analyzed results and MLT, DPD and DGM wrote the manuscrip.

12. Supplementary Information

12.1. Image Processing of Nuclei channel

The first step in the image processing is to define the dimensions of the mask used for local operations, often refereed as the kernel size (KS). Determining the optimal KS is essential for achieving accurate and reliable image quantification by effectively balancing noise reduction, feature enhancement, edge preservation, computational efficiency, and consistency across datasets.

We have designed a method to estimate the optimal KS automatically through the following steps: (1) First, the most densely populated confocal plane in the 3D image (i.e., the plane with the highest number of objects) is identified by searching for the confocal plane with the highest mean intensity. (2) This plane undergoes signal thresholding, where values below the average intensity of the sample are considered as background. (3) Subsequently, a median filter with a window size of 1 pixel is applied. (4) Following this, the Euclidean Distance Transform (EDT) is computed, and local maxima are identified. (5) Finally, the average object radius is estimated from the average distances between local maxima. This average radius is then established as the KS for processing the entire 3D image using the method described below:

- A copy of the To-Pro3 channel is processed with a Gaussian blur, minimum, and maximum filter using a value of $2xKS$.

- The resulting image is then subtracted from the original To-Pro3 channel to remove background.

- Next, a standard binary morphological opening operation is applied on the resulting image. This operation removes small objects while connecting existing ones, improving segmentation accuracy.

- Next, a basic 2D watershed algorithm is applied to each section of the image to outline the object borders in XY.

The previous set of instructions are performed automatically as a script with no free parameters, and the resulting image is now ready to be processed by OSCAR, as explained in the next section.

12.2. Object Statistical Clustering of Adjacent Regions (OSCAR) Pipeline

This section presents an in-depth overview of the sequential procedures integrated within the Object Statistical Clustering of Adjacent Regions (OSCAR) framework for reconstructing objects in three-dimensional space using data from confocal planes. In essence, OSCAR operates by processing the bounding boxes of individual objects in a confocal section of the image and fitting them as parametric functions. These parametric functions (referred to as 2D-Objects from now on), are then clustered based on defined interactions with the 2D-Objects in adjacent confocal planes in a sequential manner. The cluster of 2D-Objects (referred to as 3D-Objects from now on) is then utilized to identify and depict the actual object it represents. The framework comprises five primary steps: (1) 2D-Object Identification, (2) 3D-Object Initiation, (3) 3D-Object Elongation, (4) 3D-Object Termination, and (5) 3D-Object Identification.

12.2.1. 2D-Object Identification

(1) The initial step is aimed at processing all planes of the 3D image to extract information about the sections of each object within the image. This involves feeding the processed 3D image (as detailed in the previous section) into an algorithm tasked with detecting individual objects in each plane. Subsequently, corresponding bounding boxes are generated for each object. (2) Each bounding boxes' contour is then inputted into an algorithm for parametric function fitting using a nonlinear least squares method. For the purpose of this study, since we are using nuclei to identify the cells, we use the ellipses as our parametric curve of interest. (3) Each fitting is identified as a 2D-Object and serves as the foundational elements for clustering. Parameters for each 2D-Object (such as center, size, axis, etc.) are stored as a single row in a matrix for each section of the image. (4) 2D-Objects smaller than $KS \times KS$ are discarded from the analysis. The remaining 2D-Objects will be utilized by the algorithms described below to reconstruct and identify the 3D-Objects within the image.

12.2.2. 3D-Object initiation

The sequential reconstruction of the 3D-Objects begins with the identification of the 2D-Objects that serve as the starting points for 3D-Objects. This process involves establishing and ranking interactions between 2D-Objects in adjacent planes of the image. The nature of these interactions and the parameters used for evaluation will vary depending on the characteristics of the image. Clear images may be ranked based on simple overlap, while more complex images may require a combination of multiple sequential methods. To achieve this, we have implemented and tested the following methods:

- Euclidean centroid distance: For each 2D-Object i in plane z i_z, we compute the distance to the k-closest 2D-Object in plane $z+1$. A 2D-Objects that has not been chosen is considered the first 2D-Object of a new 3D-Object (Supplementary Figure 4A, red ellipse).

- Overlapping Area: For each 2D-Object i in plane z i_z, we compute the number of pixels that overlap with the 2D-Objects in plane $z+1$. A point (x, y) in ellipse j_{z+1} with foci $F_1 = (x_1, y_1)$, $F_2 = (x_2, y_2)$, and major axis a_i is inside ellipse i_z if:

$$\sqrt{(x - x_1)^2 + (y - y_1)^2} + \sqrt{(x - x_2)^2 + (y - y_2)^2} \leq 2a_i \tag{3}$$

  A 2D-Object that does not have maximum overlap with any 2D-Object in the plane above is considered the first 2D-Object of a new 3D-Object (Supplementary Figure 4B, red ellipse).

- Percentage of intersecting area (Supplementary Figure 4C): To correct for bias towards establishing connections between ellipses of larger size (that may overlap more with ellipses in planes above), we compute $U_{i,j}$ (% of area of i inside j) and $U_{j,i}$ (% of area of j inside i). Then the intersection index is defined as:

$$II_{i,j} = \frac{U_{i,j}}{Area_i} \cdot \frac{U_{j,i}}{Area_j} = \frac{U_{i,j}^2}{Area_i \cdot Area_j} \tag{4}$$

  which is true because $U_{i,j} = U_{j,i}$. Therefore, the algorithm only requires a single computation of the overlapping area. A 2D-Object that does not have maximum percentage of intersection with any 2D-Object in the plane above is considered the first 2D-Object of a new 3D-Object.

- Percentage of perimeter: An alternative method (that yields similar results but it at lower computational cost) uses the percentage of perimeter of the 2D-Object in z that is inside the 2D-Object in $z + 1$. Now, a 2D-Object that does not have maximum percentage of perimeter with any 2D-Object in the plane above is considered the first 2D-Object of a new 3D-Object.

- 3D-Object trajectory (Supplementary Figure 4D): the centroids of the 2D-Objects of each 3D-Object are used to fit a line that predict its potential location in the plane $z + 1$. 3D fitting is performed by using the "least squares method" in two spatial directions: x-axis over z-axis; and y-axis over z-axis. Using the parameters obtained from both fittings, we can calculate a new line as the intersection between these two planes [93]. 2D-Objects in plane $z + 1$ are then ranked based on euclidean distance to the projection of this line in this plane. A 2D-Object not chosen as closest to any 3D-Object trajectory is considered the first 2D-Object of a new 3D-Object (Supplementary Figure 4D, red ellipse).

A critical factor in determining object connections relies heavily on the quality of the image in all three spatial orientations. In scenarios where images exhibit a high signal-to-noise ratio, each ellipse is exclusively associated with a single 3D-Object (as illustrated in Supplementary Figure 4E). However, challenges emerge in less optimal images where segmentation errors are unavoidable.

To tackle this issue, we permit each 2D-Object to contribute to multiple 3D-Objects concurrently (as demonstrated in Supplementary Figure 4F). This approach enables the framework to overcome potential under-segmentation errors common in dense images. Conversely, such promiscuity may lead to conflicts when false objects (over-segmentation) occur due to excessive object segmentation. Nevertheless, this risk is mitigated by implementing strict criteria when defining 2D-Object initiators, which are always considered non-promiscuous. In this study, we use sequential weighted combination of "Percentage of perimeter" and "3D-Object trajectory", while allowing for 2D-Object promiscuity. In this scenario, each 2D-Object can be chosen as part of several 3D-Object, and each 2D-Object not chosen is considered the first 2D-Object of a new 3D-Object.

12.2.3. 3D-Object elongation

Next, for a given 2D-Object labeled as a seed z, the 3D-Object is elongated by sequential ranking and selection of the 2D-Objects in planes $z + 1$ and beyond, based again in the interactions described above. Again, the "3D-Object projection" is used to utilize the three-dimensional information from the planes above to mitigate segmentation errors in dense images. Alternatively, to minimize error accumulation, the "3D-Object trajectory" can be calculated based only on the centroids of the first k 2D-Objects. In this study, k is set as half of the average size in z of the 3D-Objects ($medZ$) calculated as follows:

- The 3D image is resampled using interpolation to generate a new image consisting on the XZ projection of the objects.

- This image is then processed by applying a Gaussian, maximum, and 2D watershed filters.

- Next, using "Analyze particles plugin" in FIJI, three key values on the objects in the z-axis are computed: minimum and maximum z-lengths ($minZ$ and $maxZ$), and average z-length ($medZ$).

- These values are then used to construct the 3D-Object Trajectories and to define the end point of each 3D-Object, as explained in the next section.

Based on the interactions described above, 3D-objects that cannot be elongated above $minZ$ are discarded from the analysis.

12.2.4. 3D-Object termination.

The final step in the 3D-Object reconstruction process is to determine when a given 2D-Object marks the end of a specific 3D-Object. In low-density images, we can consider an endpoint as the 2D-Object that is part of a 3D-Object and does not interact with another 2D-Object below, according to the interactions defined previously (Supplementary Figure 5A). However, in dense realistic images, this condition is rarely met (objects are so close that there is always some overlapping between section in consecutive planes), necessitating alternative strategies to define the termination of 3D-Objects (Supplementary Figure

5B). These strategies rely on statistical analysis and curve fitting to ascertain the integrity of each 3D-Object. When a given 3D-Object reaches a length in z between $medZ$ and $maxZ$, its integrity is computed based on three parameters:

- The average distance of the centroids of the 2D-Object to the 3D-Object line (as defined above)

- The angle between the 3d projection line and the vectors formed by two consecutive centroids

- The cumulative Pearson Correlation Coefficient ρ between the two previous variables.

This last strategy is the one used in the present contribution. This way, in well defined 3D-Objects with high integrity, both distance and angle should remain close to zero, and $\rho \approx 1$ (the two variables are perfectly linearly correlated). On the other hand, in 3D-Objects with low integrity (very noisy), angle and distance increase in value and become uncorrelated ($\rho \to 0$) as more 2D-Objects are added to the 3D-Object. To find the termination in these conditions, the algorithm proceeds as follows:

- Centroids of 2D-Objects that are outside a 50% confidence interval of the fitting that generates the '3D-Object trajectory" in both distance and angle are labeled as *outliers*. Then, we compute the number of *outliers* whose indexes are before ($c_{in} = \sum_{z=1}^{z_{mean}} C_z^+$) or after ($c_{out} = \sum_{z=z_{mean}+1}^{n} C_z^-$) $medZ$ value.

- When the number of *outliers* after $medZ$ is higher before $medZ$, the integrity of the 3D-Object is labeled as "ok". In this situation, the value of the Pearson Correlation Coefficient of the 3D-Object before the *outlier* is higher than its value of the whole 3D-Object, we establish this 2D-Object as the end plane of the 3D-Object (Supplementary Figure 5C). The rationale behind this method is based in the fact that, for sharp 3D-Objects, the terminator corresponds to the last centroid that lies inside the confidence interval (illustrated as the cylinder in Supplementary Figure 5C-D), while in noisy objects, some centroids in the first $medZ$ sections can be outside the confidence interval, so the cut occurs when more centroids after $medZ$ are outside CI than in the first $medZ$ planes (illustrated in Supplementary Figure 5D).

- On the other hand, when the number of outliers before $medZ$ is lower than after $medZ$, the integrity of the 3D-Object is labeled as "compromised" (the termination of the 3D-Object cannot be established based on this method). In this situation (a potential scenario typical of really dense images with very poor signal-to-noise ratio), we define the termination of the 3D-Object at $medZ$.

29

12.2.5. 3D-Object identification

Once all 3D-Objects are identified and located, the additional channels of the image can be computed and processed to determine the identity of cells based on labeling of interest. For example, if each color channel corresponds to a different immunostaining, we can establish a particular fate (such as progenitors P, differentiated D, intermediate progenitors IP, quiescent or apoptotic) based on comparison between average intensity levels.

Single-labeled images require the definition of a threshold , to differentiate between signal (intensity values above a threshold) versus background (intensity values below a threshold). This threshold is automatically calculated suing the following steps: (1) The image is processed similarly to the ToPro3 processing (see Image Processing of Nuclei channel Section in this Supplemntary Information). (2) An additional background subtraction performed. (3) The median of pixel intensity values is calculated using the full pixel intensity histogram (cutoff value). (4) Pixels with an intensity value lower than the cutoff value are discarded. (5) A new median value is calculated and used to delineate the boundary between the background (pixels with lower intensity) and the foreground (pixels with higher intensity) for each confocal plane of the image. This process is repeated for every confocal slice. In the present study, this approach was used for Pcna, pHH3, and Active Caspase 3.

Alternatively, when two complementary stainings are used (where cells positive for one staining should be negative for the other and vice versa, automated identification of 3D-Object identity can be achieved without the need for a threshold, by simple integration and comparison of intensity levels between the two normalize signals in all 2D-Objects that compose the 3D-Object. This approach was used in the present study to classify cell fate as P, D or IP based on Atoh7 and Sox2 levels.

12.2.6. Algorithm availability and Description

Code generated and used as part of the present manuscript available for download in the following link: https://github.com/davidgmiguez/OSCAR.

Pseudo-code for OSCAR is schematized below:

Data: Data2D = 2D processing and identification
Data: calculation of minZ, medZ,maxZ
Result: 3D-Object construction
for *2D-Object* **in** *Data2D* **do**
    if *2D-Object = initiator* **then**
        while *3D-Object length < maxZ* **do**
            3D-Object elongation
        end
        if *3D-Object length ≥ minZ* **then**
            if *3D-Object length > medZ* **then**
                3D-Object termination
            end
        end
    end
end

Algorithm 1: OSCAR Pseudocode

12.2.7. Generation of 3D Digital Tissues and "Ground Truth" Comparison

To evaluate OSCAR's accuracy compared to other tested tools in imperfect images, we used computer-generated images where the number and location of all objects in the sample are known, and density and overlap can be modulated as desired. To generate these images, we developed an algorithm in the Julia programming language (available as Supplemental Information), where 2500 volumetric objects (ellipsoids in this example) are placed in a limited region of 200 μm in width, height, and depth. The size, shape, and orientation of each ellipsoid are determined from gamma distributed values, with a median of 6 μm, a 30% standard deviation, and random orientation along one of the three axes.

In less-than-ideal images from dense biological tissues, individual objects often appear overlapped, making image segmentation challenging. To simulate this, we allow each object to overlap by a maximum of 10% with neighboring objects. These objects are then represented using the Fiji plugin "3D Draw Shape" [89, 88], with voxel dimensions set to 1 μm. Next, the resulting image undergoes processing to reduce the signal-to-background ratio along one axis, similar to realistic biological images reconstructed from confocal sections. This is achieved by applying a grayscale morphological dilation operation and Gaussian noise across one axis. Additionally, to mimic reduced resolution in all dimensions, we process the image by adding a normalized version of the inverted original image to itself, resulting in an image that simulates the out-of-focus light scattering effect around each object.

Three independent 3D images for each condition are generated and processed with OSCAR and the following free and commercial software solutions.

Object Counter 3D (OC3D) is an open-source algorithm implemented in Fiji [94] based on voxel connectivity to perform teh segmentation. In other words, OC3D identifies a single 3D-Object as all voxels with an intensity value higher than a certain cutoff value (foreground) that are connected without interruption by voxels with intensity values below the cutoff (background). The

detection of the background marks the end of a detected 3D-Object.

TANGO, or "3D analysis" plugin is part of the 3D ImageJ Suite package of Fiji. Contrary to OC3D, TANGO incorporates the centroid to calculate spatial and morphological measurements [88]. TANGO specifically works with images where 3D-Objects have been previously identified and labeled. Each label corresponds to a specific voxel intensity associated with only one 3D-Object, allowing TANGO to identify them directly from the histogram of voxel intensities. In this comparison, both TANGO and OC3D utilize input images previously segmented using the 3D-watershed algorithm from the 3D ImageJ Suite package.

Imaris© 8 is a commercial platform for image visualization, processing, and analysis, widely adopted by the scientific community for its user-friendly interface and extensive toolset. Data from Imaris is utilized by activating the segmentation step and the 3D detection tool, which are commonly employed in various studies [12].

Huygens© Professional version 19.04 is another widely used commercial platform in the contect of 3D image analysis. The images were analyzed using the Huygens Object Analyzer © tool, which simplifies segmentation by optimizing seed and threshold levels with algorithms, providing instant feedback such as the number of objects per channel.

12.2.8. Accuracy Comparison in the 3D space

As explained earlier, one of the main advantages of OSCAR is that it does not require any input parameters from the user. However, to perform a fair comparison with other tools that do require the radius of the object in 3D as input, the average length of nuclei in the z dimension is fixed at 12 μm for all tools.

To evaluate accuracy in number of detected objects, we use the following formula:

$$(1 - \frac{|Number\ of\ real\ objects - Number\ of\ found\ objects\ -}{Number\ of\ real\ objects}) \cdot 100$$

To evaluate accuracy in spatial location, we utilize the Friedmann-Rafsky (FR) test [95]. This statistical method tests whether two point clouds belong to the same distribution. The test is an extension of the Wald-Wolfowitz runs test for dimensions greater than one and is based on computing the Minimum-Spanning Tree (MST). In essence, the algorithm generates a connected, edge-weighted, and undirected graph from two sets of points distributed in 3D space. Each pair of nodes is connected in a way that ensures all vertices remain connected without forming any cycles, while minimizing the total Euclidean distance of the graph (considered as the weight of the edges connecting the nodes). Then, the number of "runs" (R) is computed as the number of edges connecting different samples plus one. Finally, the FR-statistic W is calculated as:

$$\frac{R - \mu}{\sigma}$$

32

being μ and σ the expectation and standard deviation of the R distribution [95, 96].

To reject the null hypothesis (i.e, both distributions follow the same distribution), the rejection p-value for significant differences between the two samples must be adjusted based on the sample size (larger samples correspond to smaller rejection p-values). However, when randomizing the sub-sample, multiple test runs are necessary to compute a median and avoid biases. Common approaches involve taking random sub-samples of equal size for both samples and running the test as many times as there are points taken. Subsequently, the rejection p-value is adjusted accordingly.

As we are not seeking to reject the null hypothesis but rather to compare normalized FR statistics for different methods, we have opted to compare 500 random centroids of the objects found against the entire set of centroids of the artificial image. Since W follows a standard normal distribution, lower values of the statistic indicate better performance; smaller values imply a higher degree of similarity between distributions [95], thus resulting in better spatial location of the detected objects.

12.3. Akaike method for best fitting estimation

To mitigate the inherent variability in cell numbers, even within samples from the same batch, multiple data points are quantified using automated tools and then fitted to parametric curves. This approach allows for deriving statistically significant conclusions. The best fitting curve is determined using Akaike weights, calculated as explained below ([90]):

$$AIC = -2log(\mathcal{L}(\hat{\theta}|data)) + 2K \tag{5}$$

that computes the logarithm of the maximum of the likelihood function of the model, and K represents the number of free parameters. Once individual values of AIC for each model are computed, the values are re-scaled to allow comparison.

$$\Delta_i = AIC_i - AIC_{min} \tag{6}$$

This way, each Δ_i can be interpreted as the information loss if the model with minimum AIC is not selected. From these values, we can then calculate the likelihood of each model given the data, with the simple transformation $exp(-\Delta_i/2)$ for each of the models. Finally, these likelihood values are normalized and treated as probabilities, as stated in [97]:

$$w_i = \frac{exp(-\Delta_i/2)}{\sum_{r=1}^{R} exp(-\Delta_r/2)} \tag{7}$$

These Akaike weights are considered as the "weights of evidence" in favor of each model as being the best under Kullback-Leibler information theory (a simple metric to measure how far a distribution is from another). Therefore, we selected the model with the highest w_i as it can be interpreted to be the most probable model given the set of data and considered models.

12.4. Delta method for error propagation

The Delta method ([91]) enables us to calculate the standard errors for the margins of a regression. It capitalizes on the property that the margin is typically an infinitely differentiable function of the data. This method employs a Taylor series expansion of the inverse link function of the regression to approximate the margin in the vicinity of the data, accomplished through three steps.

- Calculate the jacobian matrix of the inverse link function of the fitting.

- Compute the variance-covariance matrix

- pre- and post-multiply the partial derivatives of the inverse link function by the original variance-covariance matrix from the regression.

This provides an estimation of the confidence interval CI of the nonlinear fitting (i.e., a 95% CI marks the range where the true fit lies in with 95% confidence).

Next, we perform numerical simulations of the branching process equations that predict the value of P and D based on the values of $pp - dd$ and T calculated experimentally [10]. Simulations are built by recursively adding to the previous number of P and D cells, a random number drawn from a gaussian distribution with mean equal to the increment predicted by the fitting, and variance corresponding to the one calculated with the Delta method.

This way, the CI of the predictions for $pp - dd$ and T (represented as ribbons in the plots) illustrate the uncertainty in the prediction propagated by the uncertainty in the number of P and D cells measured (higher dispersion in the experimental data results in larger CI that results in higher uncertainty in the value of $pp - dd$ and T predicted by the branching).

References

[1] C. L. Cepko, C. P. Austin, X. Yang, M. Alexiades, D. Ezzeddine, Cell fate determination in the vertebrate retina., Proceedings of the National Academy of Sciences of the United States of America 93 (2) (1996) 589–595. doi:10.1073/pnas.93.2.589.
URL http://dx.doi.org/10.1073/pnas.93.2.589

[2] J. He, G. Zhang, A. D. Almeida, M. Cayouette, B. D. Simons, W. A. Harris, How variable clones build an invariant retina., Neuron 75 (5) (2012) 786–798. doi:10.1016/j.neuron.2012.06.033.
URL http://dx.doi.org/10.1016/j.neuron.2012.06.033

[3] D. Pérez-Dones, M. Ledesma-Terrón, D. G. Míguez, Quantitative Approaches to Study Retinal Neurogenesis, Biomedicines 9 (9) (2021) 1222. doi:10.3390/biomedicines9091222.
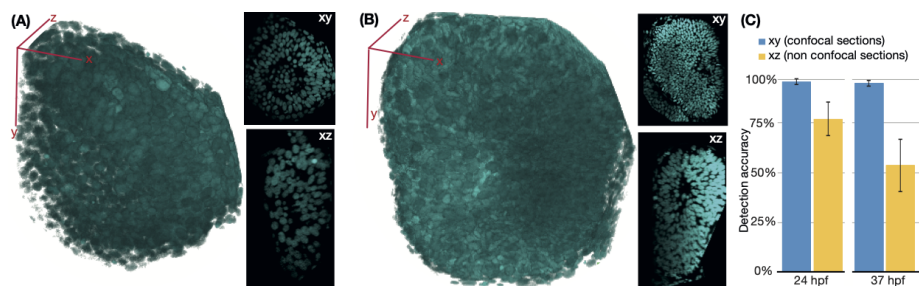URL https://www.mdpi.com/2227-9059/9/9/1222

Figure 8: *

Supplementary Figure 1: Detection accuracy in artificial images of different noise levels after 2D watershed. (A-B) 3D projection of retinas imaged *in toto* and stained with ToPro3 at (A) 24 and (B) 37 hours post fertilization (hpf). Confocal (*xy*, high resolution, upper panel) and non-confocal (*xz*, low resolution, lower panel) are shown to illustrate the reduced resolution that compromises the segmentation of the image in three dimensions. (C) quantification of the detection accuracy in terms of number of nuclei in confocal (blue) and nonconfocal (yellow) planes in the central plane of the images in (A,B) using FIJI stock algorithms for 2D watershed. Segmentation accuracy is very good in *xy*, but it is highly reduced in the *xz* section. This low accuracy results in reduced resolution when using automated segmentation of the full 3D image.

Stage (hpf)	Incubation time(min)
20	10
22	12
24	14
26	16
28	18
30	20
32	23
34	25
36	28
38	31
40	33
42	36
44	39
46	42
48	45

Table 1: *

Supplementary Table 1: Proteinase K exposure times for different stages.
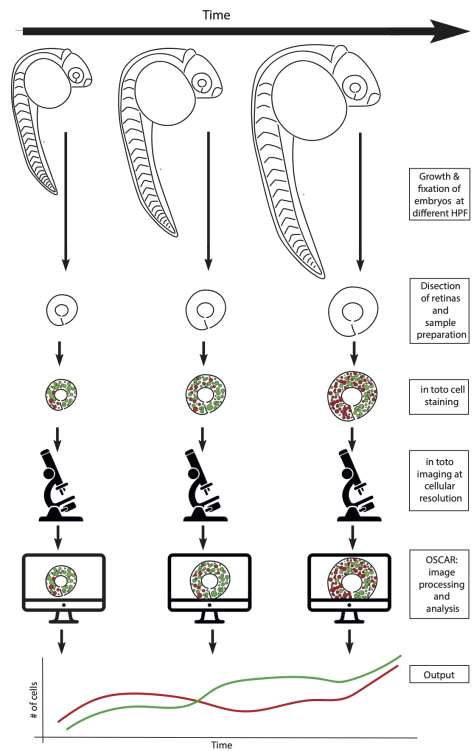
Figure 9: *

Supplementary Figure 2: Scheme of the experimental protocol: Embryos are allowed to develop in normal conditions and fixed at different time points. Retinas are then dissected, and immunofluorescence is performed *in toto* using the combination of antibodies and/or fluorescent staining desired for each experiment. Next, retinas are imaged *in toto* in a confocal microscope with 30% overlap between planes to obtain an optimal 3D reconstruction of the tissue. Finally, the multiple independent repeats for each condition and time-point are processed and quantified using OSCAR. Output of OSCAR is used to monitor key features of the development of the Zebrafish retina, such as density, number of cells and used as input of branching equations to study the balance between proliferation and differentiation dynamics.
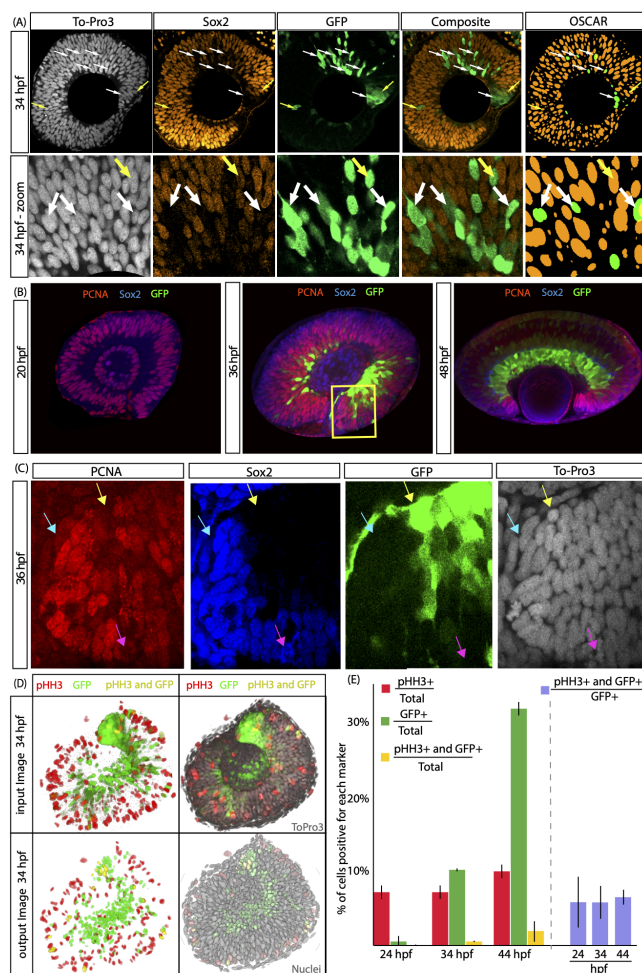
Figure 10: *

Supplementary Figure 3: The identity of the cells in the zebrafish retina can be established based on the combination between immunostaining intensities. (A) Different channels of an image of a representative section of a developing retina at 34 hpf. A zoom of each image is shown below, to illustrate cells positive and negative for each staining. (B) Central slices of retinas at three different developmental stages, co-stained with Pcna (red), Sox2(Blue) and GFP (green). (C) Zoom of a region of the 36hpf retina. Channels are split to see differences between stains. Yellow arrows point to a nuclei negative for Pcna and Sox2 and positive for GFP. Pink arrows point to a dividing nuclei negative for Pcna and GFP and positive for Sox2. Cyan arrows point to a quiescent nuclei, negative for Pcna and GFP and positive for Sox2. (D) 3D-view projections of the input image, zebrafish retina imaged in toto at 34 hpf stained with pHH3 (red), GFP+ (green), double positive for pHH3 and GFP (yellow) and To-Pro3 (grey). Below each image, the corresponding output from the automated quantification. (E) Percentage of cells that are pHH3+ (red column), GFP+ (green column) and double positive for pHH3 and GFP (yellow column). In purple, percentage of GFP+ that are both GFP+ and pHH3+ at different time points remains around 7%.

37
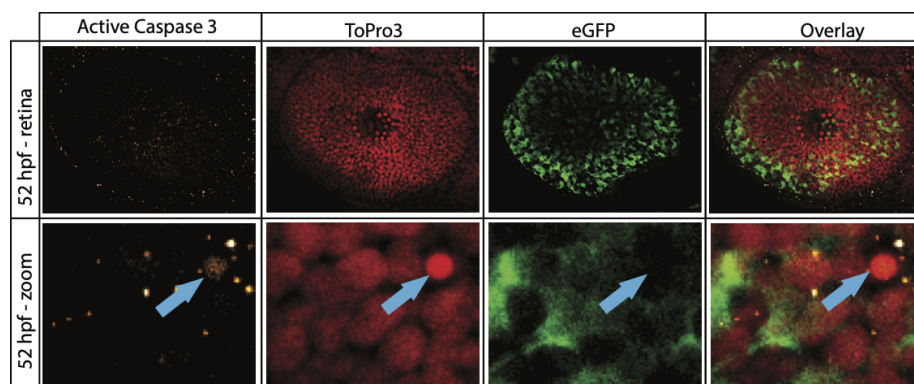
Figure 11: *

Supplementary Figure 4: Positive control for Active Caspase 3 immunostaing. 3D projection of a zebrafish retina at 52 hpf imaged *in toto* as positive control showing cells positive for immunostaining against Active Caspase 3. Imaged in row below illustrates a cell (blue arrow) with positive staining for Active Caspase 3 (smaller dots are processed as background signal of the antibody by OSCAR, and only larger dots that overlap with nuclei are considered as cells undergoing apoptosis).

Drugs		
Name	Ref.	Working Conc.
Cyclopamine V	Merck 239806	0.1mM
XAV939	Merck 575545	0.1mM
DAPT	Merck 565784	0.05mM
SU5402	Merck 572630	0.025mM

Table 2: *

Supplementary Table 2: Inhibitor concentrations used.

Z-Test p values		
Drug	p-value T	p-value D
Cyclopamine	0.21	3.83E-15
XAV939	1.87E-7	8.36E-19
DAPT	0.0017	4.26E-11
SU5402	0.0022	2.55E-30

Table 3: *

Supplementary Table 3: p-values to illustrate significant differences between estimated coefficients of control conditions against each drug treatment.
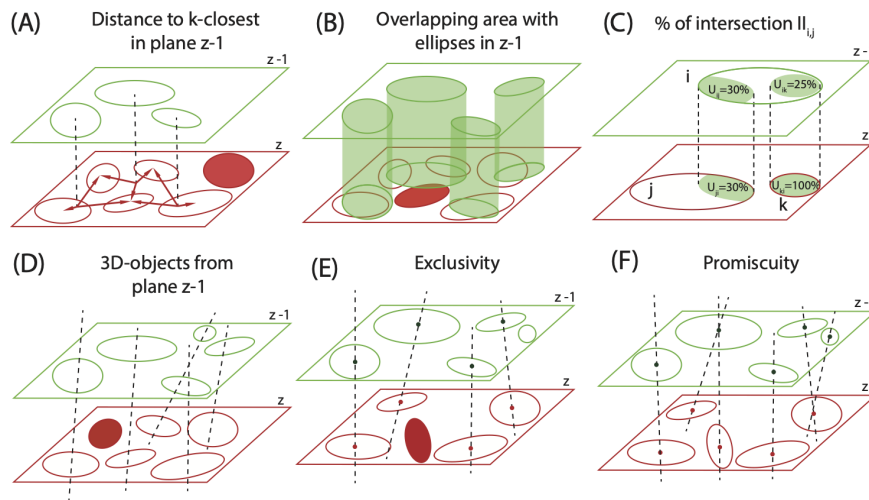
Figure 12: *

Supplementary Figure 4: Interactions between 2D-Objects and elongation of 3D-Objects. (A-D) Identification of 2D-object in plane z interactions based on. (A) Euclidean distance, (B) Overlap, (C) percentage overlap and (D) distance to teh projection of the "3D-Object trayectory". 2D-Objects that are not part of any previously formed 3D-Object are labeled in red and identified as seeds of a new 3D-Object. (E-D) Types of interactions (E) exclusive (each 2D-Object can be only part of a single 3D-Object) or (F) promiscuous (each 2D-Object is allowed to be part of multiple 3D-Objects).

Root Mean Squared Errors		
Drug	RMSE	RMSE*
Cyclopamine	2092	2639
XAV939	1922	1949
DAPT	1905	2301
SU5402	1312	1313

Table 4: *

Supplementary Table 4: RMSE with fitting modification or without fitting modification(*).
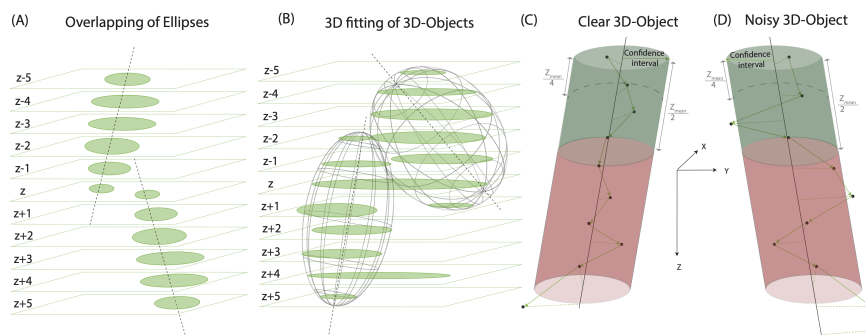
Figure 13: *

Different approaches to establish terminal sections of a 3D-Object.
(A) In well defined images, the last ellipse of a 3D-Object that does not interact with an ellipse in the following plane is considered the terminal sections of a 3D-Object. (B) In less ideal images, the first half of the 3D-Object is fitted to a 3d-parametric curve. The ellipse at the plane marked by the fitting is identified as the terminal last section of the 3D-Object. (C) Identification of terminators based on confidence intervals. The last centroid inside the confidence interval establishes the last section of the 3D-Object. (D) For very noisy objects, the final point is established when more centroids after the average half side are outside the confidence interval than before the average half size of the 3D-Objects.

[4] V. Graham, J. Khudyakov, P. Ellis, L. Pevny, SOX2 functions to maintain neural progenitor identity., Neuron 39 (5) (2003) 749–765. doi:10.1016/s0896-6273(03)00497-5.
URL http://dx.doi.org/10.1016/s0896-6273(03)00497-5

[5] A. D. Almeida, H. Boije, R. W. Chow, J. He, J. Tham, S. C. Suzuki, W. A. Harris, Spectrum of Fates: a new approach to the study of the developing zebrafish retina., Development 141 (9) (2014) 1971–1980. doi:10.1242/dev.104760.
URL http://dx.doi.org/10.1242/dev.104760

[6] L. Poggi, M. Vitorino, I. Masai, W. A. Harris, Influences on neural lineage and mode of division in the zebrafish retina in vivo., The Journal of Cell Biology 171 (6) (2005) 991–999. doi:10.1083/jcb.200509098.
URL http://dx.doi.org/10.1083/jcb.200509098

[7] E. Nerli, M. Rocha-Martins, C. Norden, Asymmetric neurogenic commitment of retinal progenitors involves Notch through the endocytic pathway, eLife 9 (2020) e60462. doi:10.7554/eLife.60462.
URL https://elifesciences.org/articles/60462

[8] M. Versaevel, T. Grevesse, S. Gabriele, Spatial coordination between cell and nuclear shape within micropatterned endothelial cells., Nature Com-

munications 3 (2012) 671. doi:10.1038/ncomms1668.
URL http://dx.doi.org/10.1038/ncomms1668

[9] F. Del Bene, A. M. Wehman, B. A. Link, H. Baier, Regulation of neurogenesis by interkinetic nuclear migration through an apical-basal notch gradient., Cell 134 (6) (2008) 1055–1065. doi:10.1016/j.cell.2008.07.017.
URL http://dx.doi.org/10.1016/j.cell.2008.07.017

[10] D. G. Míguez, A Branching Process to Characterize the Dynamics of Stem Cell Differentiation, Scientific Reports 5 (1) (2015) 13265. doi:10.1038/srep13265.
URL https://www.nature.com/articles/srep13265

[11] M. Ledesma-Terrón, N. Peralta-Cañadas, D. G. Míguez, FGF2 modulates simultaneously the mode, the rate of division and the growth fraction in cultures of radial glia, Development 147 (14) (2020) dev189712. doi:10.1242/dev.189712.
URL https://journals.biologists.com/dev/article/147/14/dev189712/224360/FGF2-modulates-simultaneously-the-mode-the-rate-of

[12] M. Matejčić, G. Salbreux, C. Norden, A non-cell-autonomous actin redistribution enables isotropic retinal growth., PLoS Biology 16 (8) (2018) e2006018. doi:10.1371/journal.pbio.2006018.
URL http://dx.doi.org/10.1371/journal.pbio.2006018

[13] E. Dzafic, P. J. Strzyz, M. Wilsch-Bräuninger, C. Norden, Centriole amplification in zebrafish affects proliferation and survival but not differentiation of neural progenitor cells., Cell reports 13 (1) (2015) 168–182. doi:10.1016/j.celrep.2015.08.062.
URL http://dx.doi.org/10.1016/j.celrep.2015.08.062

[14] G. B. Carballo, J. R. Honorato, G. P. F. de Lopes, T. C. L. d. S. E. Spohr, A highlight on Sonic hedgehog pathway., Cell Communication and Signaling 16 (1) (2018) 11. doi:10.1186/s12964-018-0220-7.
URL http://dx.doi.org/10.1186/s12964-018-0220-7

[15] M. Placzek, J. Briscoe, Sonic hedgehog in vertebrate neural tube development, The International Journal of Developmental Biology 62 (1-2-3) (2018) 225–234. doi:10.1387/ijdb.170293jb.
URL http://www.intjdevbiol.com/paper.php?doi=170293jb

[16] M. Saade, I. Gutiérrez-Vallejo, G. LeDréau, M. A. Rabadán, D. G. Miguez, J. Buceta, E. Martí, G. Le Dréau, M. A. Rabadán, D. G. Miguez, J. Buceta, Sonic Hedgehog Signaling Switches the Mode of Division in the Developing Nervous System, Cell reports 4 (2013) 492–503. doi:10.1016/j.celrep.2013.06.038.

[17] D. G. Míguez, V. K. Vanag, I. R. Epstein, Fronts and pulses in an enzymatic reaction catalyzed by glucose oxidase., Proceedings of the

National Academy of Sciences of the United States of America 104 (17) (2007) 6992–7. doi:10.1073/pnas.0611438104.
URL http://www.pubmedcentral.nih.gov/articlerender.fcgi?artid=1855356&tool=pmcentrez&rendertype=abstract

[18] C. J. Neumann, C. Nuesslein-Volhard, Patterning of the zebrafish retina by a wave of sonic hedgehog activity., Science 289 (5487) (2000) 2137–2139. doi:10.1126/science.289.5487.2137.
URL http://dx.doi.org/10.1126/science.289.5487.2137

[19] S. W. Choy, S. H. Cheng, Hedgehog Signaling, in: Vitamins & Hormones, Vol. 88, Elsevier, 2012, pp. 1–23. doi:10.1016/B978-0-12-394622-5.00001-8.
URL https://linkinghub.elsevier.com/retrieve/pii/B9780123946225000018

[20] I. Masai, M. Yamaguchi, N. Tonou-Fujimori, A. Komori, H. Okamoto, The hedgehog-PKA pathway regulates two distinct steps of the differentiation of retinal ganglion cells: the cell-cycle exit of retinoblasts and their neuronal maturation., Development 132 (7) (2005) 1539–1553. doi:10.1242/dev.01714.
URL http://dx.doi.org/10.1242/dev.01714

[21] J. J. Lee, D. P. von Kessler, S. Parks, P. A. Beachy, Secretion and localized transcription suggest a role in positional signaling for products of the segmentation gene hedgehog., Cell 71 (1) (1992) 33–50. doi:10.1016/0092-8674(92)90264-d.
URL http://dx.doi.org/10.1016/0092-8674(92)90264-d

[22] D. García-Morales, T. Navarro, A. Iannini, P. S. Pereira, D. G. Míguez, F. Casares, Dynamic Hh signalling can generate temporal information during tissue patterning., Development 146 (8) (Apr. 2019). doi:10.1242/dev.176933.
URL http://dx.doi.org/10.1242/dev.176933

[23] D. G. Míguez, D. García-Morales, F. Casares, Control of size, fate and time by the Hh morphogen in the eyes of flies, in: Current Topics in Developmental Biology, Vol. 137, Elsevier, 2020, pp. 307–332. doi:10.1016/bs.ctdb.2019.10.011.
URL https://linkinghub.elsevier.com/retrieve/pii/S0070215319300869

[24] D. G. Míguez, A. Iannini, D. García-Morales, F. Casares, The effects of Hh morphogen source movement on signaling dynamics, Development (2022) dev.199842doi:10.1242/dev.199842.
URL https://journals.biologists.com/dev/article/doi/10.1242/dev.199842/281295/Patterning-on-the-move-the-effects-of-Hh-morphogen

42

[25] Z. Chen, X. Li, C. Desplan, Deterministic or stochastic choices in retinal neuron specification., Neuron 75 (5) (2012) 739–742. doi:10.1016/j.neuron.2012.08.008.
URL http://dx.doi.org/10.1016/j.neuron.2012.08.008

[26] D. L. Stenkamp, R. A. Frey, S. N. Prabhudesai, P. A. Raymond, Function for Hedgehog genes in zebrafish retinal development., Developmental Biology 220 (2) (2000) 238–252. doi:10.1006/dbio.2000.9629.
URL http://dx.doi.org/10.1006/dbio.2000.9629

[27] C. Y. Logan, R. Nusse, The Wnt signaling pathway in development and disease., Annual Review of Cell and Developmental Biology 20 (2004) 781–810. doi:10.1146/annurev.cellbio.20.010403.113126.
URL http://dx.doi.org/10.1146/annurev.cellbio.20.010403.113126

[28] E. M. Lad, S. H. Cheshier, M. Y. S. Kalani, Wnt-Signaling in Retinal Development and Disease, Stem Cells and Development 18 (1) (2009) 7–16. doi:10.1089/scd.2008.0169.
URL https://www.liebertpub.com/doi/10.1089/scd.2008.0169

[29] H. Yi, R. E. I. Nakamura, O. Mohamed, D. Dufort, A. S. Hackam, Characterization of Wnt Signaling during Photoreceptor Degeneration, Investigative Opthalmology & Visual Science 48 (12) (2007) 5733. doi:10.1167/iovs.07-0097.
URL http://iovs.arvojournals.org/article.aspx?doi=10.1167/iovs.07-0097

[30] J. R. Meyers, L. Hu, A. Moses, K. Kaboli, A. Papandrea, P. A. Raymond, beta-catenin-Wnt signaling controls progenitor fate in the developing and regenerating zebrafish retina., Neural Development 7 (2012) 30. doi:10.1186/1749-8104-7-30.
URL http://dx.doi.org/10.1186/1749-8104-7-30

[31] F. Osakada, S. Ooto, T. Akagi, M. Mandai, A. Akaike, M. Takahashi, Wnt Signaling Promotes Regeneration in the Retina of Adult Mammals, The Journal of Neuroscience 27 (15) (2007) 4210–4219. doi:10.1523/JNEUROSCI.4193-06.2007.
URL https://www.jneurosci.org/lookup/doi/10.1523/JNEUROSCI.4193-06.2007

[32] A. V. Sanchez-Sanchez, E. Camp, A. Leal-Tassias, J. L. Mullor, Wnt signaling has different temporal roles during retinal development, Developmental Dynamics (2009) n/a–n/adoi:10.1002/dvdy.22168.
URL https://onlinelibrary.wiley.com/doi/10.1002/dvdy.22168

[33] T. J. Van Raay, M. L. Vetter, Wnt/frizzled signaling during vertebrate retinal development., Developmental Neuroscience 26 (5-6) (2004) 352–358.

43

doi:10.1159/000082277.
URL http://dx.doi.org/10.1159/000082277

[34] R. U. Iongh, De, WNT/Frizzled signaling in eye development and disease, Frontiers in Bioscience 11 (1) (2006) 2442. doi:10.2741/1982.
URL https://imrpress.com/journal/FBL/11/3/10.2741/1982

[35] S.-M. A. Huang, Y. M. Mishina, S. Liu, A. Cheung, F. Stegmeier, G. A. Michaud, O. Charlat, E. Wiellette, Y. Zhang, S. Wiessner, M. Hild, X. Shi, C. J. Wilson, C. Mickanin, V. Myer, A. Fazal, R. Tomlinson, F. Serluca, W. Shao, H. Cheng, M. Shultz, C. Rau, M. Schirle, J. Schlegl, S. Ghidelli, S. Fawell, C. Lu, D. Curtis, M. W. Kirschner, C. Lengauer, P. M. Finan, J. A. Tallarico, T. Bouwmeester, J. A. Porter, A. Bauer, F. Cong, Tankyrase inhibition stabilizes axin and antagonizes Wnt signalling, Nature 461 (7264) (2009) 614–620. doi:10.1038/nature08356.
URL https://www.nature.com/articles/nature08356

[36] D. M. Ornitz, N. Itoh, The Fibroblast Growth Factor signaling pathway, WIREs Developmental Biology 4 (3) (2015) 215–266. doi:10.1002/wdev.176.
URL https://wires.onlinelibrary.wiley.com/doi/10.1002/wdev.176

[37] B. Zhou, W. Lin, Y. Long, Y. Yang, H. Zhang, K. Wu, Q. Chu, Notch signaling pathway: architecture, disease, and therapeutics, Signal Transduction and Targeted Therapy 7 (1) (2022) 95. doi:10.1038/s41392-022-00934-y.
URL https://www.nature.com/articles/s41392-022-00934-y

[38] R. I. Dorsky, D. H. Rapaport, W. A. Harris, Xotch inhibits cell differentiation in the xenopus retina, Neuron 14 (3) (1995) 487–496. doi:10.1016/0896-6273(95)90305-4.
URL https://linkinghub.elsevier.com/retrieve/pii/0896627395903054

[39] S.-i. Ohnuma, A. Philpott, K. Wang, C. E. Holt, W. A. Harris, p27Xic1, a Cdk Inhibitor, Promotes the Determination of Glial Cells in Xenopus Retina, Cell 99 (5) (1999) 499–510. doi:10.1016/S0092-8674(00)81538-X.
URL https://linkinghub.elsevier.com/retrieve/pii/S009286740081538X

[40] S.-i. Ohnuma, S. Hopper, K. C. Wang, A. Philpott, W. A. Harris, Coordinating retinal histogenesis: early cell cycle exit enhances early cell fate determination in the *Xenopus* retina, Development 129 (10) (2002) 2435–2446. doi:10.1242/dev.129.10.2435.
URL https://journals.biologists.com/dev/article/129/10/2435/41716/Co-ordinating-retinal-histogenesis-early-cell

[41] Z.-D. Zhou, U. Kumari, Z.-C. Xiao, E.-K. Tan, Notch as a molecular switch in neural stem cells, IUBMB Life 62 (8) (2010) 618–623. doi:10.1002/iub.362.
URL https://onlinelibrary.wiley.com/doi/10.1002/iub.362

[42] D. A. Greenberg, K. Jin, Turning neurogenesis up a Notch, Nature Medicine 12 (8) (2006) 884–885. doi:10.1038/nm0806-884.
URL https://www.nature.com/articles/nm0806-884

[43] R. R. Katreddi, E. Z. M. Taroc, S. M. Hicks, J. M. Lin, S. Liu, M. Xiang, P. E. Forni, Notch signaling determines cell-fate specification of the two main types of vomeronasal neurons of rodents, Development 149 (13) (2022) dev200448. doi:10.1242/dev.200448.
URL https://journals.biologists.com/dev/article/149/13/dev200448/275904/Notch-signaling-determines-cell-fate-specification

[44] S. Tagami, M. Okochi, K. Yanagida, A. Ikuta, A. Fukumori, N. Matsumoto, Y. Ishizuka-Katsura, T. Nakayama, N. Itoh, J. Jiang, K. Nishitomi, K. Kamino, T. Morihara, R. Hashimoto, T. Tanaka, T. Kudo, S. Chiba, M. Takeda, Regulation of Notch Signaling by Dynamic Changes in the Precision of S3 Cleavage of Notch-1, Molecular and Cellular Biology 28 (1) (2008) 165–176. doi:10.1128/MCB.00863-07.
URL https://www.tandfonline.com/doi/full/10.1128/MCB.00863-07

[45] S. Artavanis-Tsakonas, K. Matsuno, M. E. Fortini, Notch Signaling, Science 268 (5208) (1995) 225–232. doi:10.1126/science.7716513.
URL https://www.science.org/doi/10.1126/science.7716513

[46] K. Henning, J. Heering, R. Schwanbeck, T. Schroeder, H. Helmbold, H. Schäfer, W. Deppert, E. Kim, U. Just, Notch1 activation reduces proliferation in the multipotent hematopoietic progenitor cell line FDCP-mix through a p53-dependent pathway but Notch1 effects on myeloid and erythroid differentiation are independent of p53, Cell Death & Differentiation 15 (2) (2008) 398–407. doi:10.1038/sj.cdd.4402277.
URL https://www.nature.com/articles/4402277

[47] T. Schroeder, U. Just, mNotch1 signaling reduces proliferation of myeloid progenitor cells by altering cell-cycle kinetics, Experimental Hematology 28 (11) (2000) 1206–1213. doi:10.1016/S0301-472X(00)00534-8.
URL https://linkinghub.elsevier.com/retrieve/pii/S0301472X00005348

[48] A. Geling, H. Steiner, M. Willem, L. Bally-Cuif, C. Haass, A gamma-secretase inhibitor blocks Notch signaling *in vivo* and causes a severe neurogenic phenotype in zebrafish, EMBO reports 3 (7) (2002) 688–694. doi:10.1093/embo-reports/kvf124.
URL https://www.embopress.org/doi/10.1093/embo-reports/kvf124

[49] K. Dorey, E. Amaya, FGF signalling: diverse roles during early vertebrate embryogenesis, Development 137 (22) (2010) 3731–3742. doi:10.1242/dev.037689.
URL https://journals.biologists.com/dev/article/137/22/3731/44062/FGF-signalling-diverse-roles-during-early

[50] M. Hernández-Bejarano, G. Gestri, L. Spawls, F. Nieto-López, A. Picker, M. Tada, M. Brand, P. Bovolenta, S. W. Wilson, F. Cavodeassi, Opposing Shh and Fgf signals initiate nasotemporal patterning of the retina, Development (2015) dev.125120doi:10.1242/dev.125120.
URL https://journals.biologists.com/dev/article/doi/10.1242/dev.125120/256835/Opposing-Shh-and-Fgf-signals-initiate-nasotemporal

[51] J.-R. Martinez-Morales, F. Del Bene, G. Nica, M. Hammerschmidt, P. Bovolenta, J. Wittbrodt, Differentiation of the Vertebrate Retina Is Coordinated by an FGF Signaling Center, Developmental Cell 8 (4) (2005) 565–574. doi:10.1016/j.devcel.2005.01.022.
URL https://linkinghub.elsevier.com/retrieve/pii/S1534580705000808

[52] S. Bouleau, H. Grimal, V. Rincheval, N. Godefroy, B. Mignotte, J.-L. Vayssière, F. Renaud, FGF1 inhibits p53-dependent apoptosis and cell cycle arrest via an intracrine pathway, Oncogene 24 (53) (2005) 7839–7849. doi:10.1038/sj.onc.1208932.
URL https://www.nature.com/articles/1208932

[53] B. Kong, J. Huang, Y. Zhu, G. Li, J. Williams, S. Shen, L. M. Aleksunes, J. R. Richardson, U. Apte, D. A. Rudnick, G. L. Guo, Fibroblast growth factor 15 deficiency impairs liver regeneration in mice, American Journal of Physiology-Gastrointestinal and Liver Physiology 306 (10) (2014) G893–G902. doi:10.1152/ajpgi.00337.2013.
URL https://www.physiology.org/doi/10.1152/ajpgi.00337.2013

[54] V. Lobjois, B. Benazeraf, N. Bertrand, F. Medevielle, F. Pituello, Specific regulation of cyclins D1 and D2 by FGF and Shh signaling coordinates cell cycle progression, patterning, and differentiation during early steps of spinal cord development, Developmental Biology 273 (2) (2004) 195–209. doi:10.1016/j.ydbio.2004.05.031.
URL https://linkinghub.elsevier.com/retrieve/pii/S0012160604004105

[55] Z. Li, M. Hu, M. J. Ochocinska, N. M. Joseph, S. S. Easter, Modulation of cell proliferation in the embryonic retina of zebrafish (Danio rerio), Developmental Dynamics 219 (3) (2000) 391–401. doi:10.1002/1097-0177(2000)9999:9999<::AID-DVDY1063>3.0.CO;2-G.
URL https://onlinelibrary.wiley.com/doi/10.1002/1097-0177(2000)9999:9999<::AID-DVDY1063>3.0.CO;2-G

[56] C. L. Limoli, R. Rola, E. Giedzinski, S. Mantha, T.-T. Huang, J. R. Fike, Cell-density-dependent regulation of neural precursor cell function., Proceedings of the National Academy of Sciences of the United States of America 101 (45) (2004) 16052–16057. doi:10.1073/pnas.0407065101.
URL http://dx.doi.org/10.1073/pnas.0407065101

[57] D. P. Kim, J. Yahav, M. Sperandeo, L. Maloney, M. McTigue, F. Lin, R. A. Clark, High cell density attenuates reactive oxygen species: Implications for in vitro assays: High cell density attenuates oxidative stress, Wound Repair and Regeneration 20 (1) (2012) 74–82. doi:10.1111/j.1524-475X.2011.00746.x.
URL https://onlinelibrary.wiley.com/doi/10.1111/j.1524-475X.2011.00746.x

[58] K. F. Harvey, X. Zhang, D. M. Thomas, The Hippo pathway and human cancer., Nature Reviews. Cancer 13 (4) (2013) 246–257. doi:10.1038/nrc3458.
URL http://dx.doi.org/10.1038/nrc3458

[59] C. Gérard, A. Goldbeter, The balance between cell cycle arrest and cell proliferation: control by the extracellular matrix and by contact inhibition., Interface focus 4 (3) (2014) 20130075. doi:10.1098/rsfs.2013.0075.
URL http://dx.doi.org/10.1098/rsfs.2013.0075

[60] L. M. Baye, B. A. Link, Interkinetic Nuclear Migration and the Selection of Neurogenic Cell Divisions during Vertebrate Retinogenesis, The Journal of Neuroscience 27 (38) (2007) 10143–10152. doi:10.1523/JNEUROSCI.2754-07.2007.
URL https://www.jneurosci.org/lookup/doi/10.1523/JNEUROSCI.2754-07.2007

[61] Y. A. Pan, T. Freundlich, T. A. Weissman, D. Schoppik, X. C. Wang, S. Zimmerman, B. Ciruna, J. R. Sanes, J. W. Lichtman, A. F. Schier, Zebrabow: multispectral cell labeling for cell tracing and lineage analysis in zebrafish., Development 140 (13) (2013) 2835–2846. doi:10.1242/dev.094631.
URL http://dx.doi.org/10.1242/dev.094631

[62] J. Icha, C. Kunath, M. Rocha-Martins, C. Norden, Independent modes of ganglion cell translocation ensure correct lamination of the zebrafish retina., The Journal of Cell Biology 215 (2) (2016) 259–275. doi:10.1083/jcb.201604095.
URL http://www.jcb.org/lookup/doi/10.1083/jcb.201604095

[63] M. Agathocleous, W. A. Harris, From Progenitors to Differentiated Cells in the Vertebrate Retina, Annual Review of Cell and Developmental Biology 25 (1) (2009) 45–69. doi:10.1146/annurev.cellbio.042308.113259.
URL https://www.annualreviews.org/doi/10.1146/annurev.cellbio.042308.113259

47

[64] C. Norden, A Fish Eye View: Retinal Morphogenesis from Optic Cup to Neuronal Lamination, Annual Review of Cell and Developmental Biology 39 (1) (2023) annurev–cellbio–012023–013036. doi:10.1146/annurev-cellbio-012023-013036.
URL https://www.annualreviews.org/doi/10.1146/annurev-cellbio-012023-013036

[65] M. Duman-Scheel, L. Weng, S. Xin, W. Du, Hedgehog regulates cell growth and proliferation by inducing Cyclin D and Cyclin E., Nature 417 (6886) (2002) 299–304. doi:10.1038/417299a.
URL http://dx.doi.org/10.1038/417299a

[66] B. Bénazéraf, Q. Chen, E. Peco, V. Lobjois, F. Médevielle, B. Ducommun, F. Pituello, Identification of an unexpected link between the Shh pathway and a G2/M regulator, the phosphatase CDC25B., Developmental Biology 294 (1) (2006) 133–147. doi:10.1016/j.ydbio.2006.02.035.
URL http://dx.doi.org/10.1016/j.ydbio.2006.02.035

[67] J. Cayuso, F. Ulloa, B. Cox, J. Briscoe, E. Martí, The Sonic hedgehog pathway independently controls the patterning, proliferation and survival of neuroepithelial cells by regulating Gli activity., Development 133 (3) (2006) 517–528. doi:10.1242/dev.02228.
URL http://dx.doi.org/10.1242/dev.02228

[68] R. Alvarez-Medina, G. Le Dreau, M. Ros, E. Martí, Hedgehog activation is required upstream of Wnt signalling to control neural progenitor proliferation., Development 136 (19) (2009) 3301–3309. doi:10.1242/dev.041772.
URL http://dx.doi.org/10.1242/dev.041772

[69] M. Komada, Sonic hedgehog signaling coordinates the proliferation and differentiation of neural stem/progenitor cells by regulating cell cycle kinetics during development of the neocortex., Congenital anomalies 52 (2) (2012) 72–77. doi:10.1111/j.1741-4520.2012.00368.x.
URL http://dx.doi.org/10.1111/j.1741-4520.2012.00368.x

[70] R. A. Rimerman, A. Gellert-Randleman, J. Diehl, Wnt1 and MEK1 Cooperate to Promote Cyclin D1 Accumulation and Cellular Transformation, Journal of Biological Chemistry 275 (19) (2000) 14736–14742. doi:10.1074/jbc.M910241199.
URL https://linkinghub.elsevier.com/retrieve/pii/S0021925819806567

[71] G. Civenni, T. Holbro, N. E. Hynes, Wnt1 and Wnt5a induce cyclin D1 expression through ErbB1 transactivation in HC11 mammary epithelial cells, EMBO reports 4 (2) (2003) 166–171. doi:10.1038/sj.embor.embor735.
URL https://onlinelibrary.wiley.com/doi/10.1038/sj.embor.embor735

[72] Y. Xu, Y. Tian, D. Tong, H. Zhang, Z. Luo, X. Shang, Y. Dong, Wnt Signaling Inhibits High-Density Cell Sheet Culture Induced Mesenchymal Stromal Cell Aging by Targeting Cell Cycle Inhibitor p27, Frontiers in Bioengineering and Biotechnology 8 (2020) 946. doi:10.3389/fbioe.2020.00946.
URL https://www.frontiersin.org/article/10.3389/fbioe.2020.00946/full

[73] D. Das, F. Lanner, H. Main, E. R. Andersson, O. Bergmann, C. Sahlgren, N. Heldring, O. Hermanson, E. M. Hansson, U. Lendahl, Notch induces cyclin-D1-dependent proliferation during a specific temporal window of neural differentiation in ES cells, Developmental Biology 348 (2) (2010) 153–166. doi:10.1016/j.ydbio.2010.09.018.
URL https://linkinghub.elsevier.com/retrieve/pii/S0012160610010821

[74] C. Ronchini, A. J. Capobianco, Induction of Cyclin D1 Transcription and CDK2 Activity by Notch [ic] : Implication for Cell Cycle Disruption in Transformation by Notch [ic], Molecular and Cellular Biology 21 (17) (2001) 5925–5934. doi:10.1128/MCB.21.17.5925-5934.2001.
URL https://www.tandfonline.com/doi/full/10.1128/MCB.21.17.5925-5934.2001

[75] I. Joshi, L. M. Minter, J. Telfer, R. M. Demarest, A. J. Capobianco, J. C. Aster, P. Sicinski, A. Fauq, T. E. Golde, B. A. Osborne, Notch signaling mediates G1/S cell-cycle progression in T cells via cyclin D3 and its dependent kinases, Blood 113 (8) (2009) 1689–1698. doi:10.1182/blood-2008-03-147967.
URL https://ashpublications.org/blood/article/113/8/1689/26066/Notch-signaling-mediates-G1S-cellcycle-progression

[76] A. Acar, A. Hidalgo-Sastre, M. K. Leverentz, C. G. Mills, S. Woodcock, M. Baron, G. M. Collu, K. Brennan, Inhibition of Wnt signalling by Notch via two distinct mechanisms, Scientific Reports 11 (1) (2021) 9096. doi:10.1038/s41598-021-88618-5.
URL https://www.nature.com/articles/s41598-021-88618-5

[77] S. Leger, M. Brand, Fgf8 and Fgf3 are required for zebrafish ear placode induction, maintenance and inner ear patterning, Mechanisms of Development 119 (1) (2002) 91–108. doi:10.1016/S0925-4773(02)00343-X.
URL https://linkinghub.elsevier.com/retrieve/pii/S092547730200343X

[78] W. A. Harris, V. Hartenstein, Neuronal determination without cell division in xenopus embryos, Neuron 6 (4) (1991) 499–515. doi:10.1016/0896-6273(91)90053-3.
URL https://linkinghub.elsevier.com/retrieve/pii/0896627391900533

[79] M. I. Willardsen, A. Suli, Y. Pan, N. Marsh-Armstrong, C.-B. Chien, H. El-Hodiri, N. L. Brown, K. B. Moore, M. L. Vetter, Temporal regulation of Ath5 gene expression during eye development, Developmental Biology 326 (2) (2009) 471–481. doi:10.1016/j.ydbio.2008.10.046.
URL https://linkinghub.elsevier.com/retrieve/pii/S0012160608013250

[80] M. L. Vetter, N. L. Brown, The role of basic helix-loop-helix genes in vertebrate retinogenesis, Seminars in Cell & Developmental Biology 12 (6) (2001) 491–498. doi:10.1006/scdb.2001.0273.
URL https://linkinghub.elsevier.com/retrieve/pii/S1084952101902733

[81] M. Westerfield, The Zebrafish Book: A Guide for the Laboratory Use of Zebrafish (Danio Rerio*), 1st Edition, Inst of Neuro Science, 1994.
URL https://www.iberlibro.com/9789994860579/Zebrafish-Book-Guide-Laboratory-Use-9994860577/plp

[82] C. B. Kimmel, W. W. Ballard, S. R. Kimmel, B. Ullmann, T. F. Schilling, Stages of embryonic development of the zebrafish., Developmental Dynamics 203 (3) (1995) 253–310. doi:10.1002/aja.1002030302.
URL http://dx.doi.org/10.1002/aja.1002030302

[83] S. Sorrells, C. Toruno, R. A. Stewart, C. Jette, Analysis of Apoptosis in Zebrafish Embryos by Whole-mount Immunofluorescence to Detect Activated Caspase 3, Journal of Visualized Experiments 82 (2013) 51060. doi:10.3791/51060.
URL https://www.jove.com/t/51060/analysis-of-apoptosis-in-zebrafish-embryos-by-whole--

[84] K. L. Cerveny, F. Cavodeassi, K. J. Turner, T. A. de Jong-Curtain, J. K. Heath, S. W. Wilson, The zebrafish flotte lotte mutant reveals that the local retinal environment promotes the differentiation of proliferating precursors emerging from their stem cell niche., Development 137 (13) (2010) 2107–2115. doi:10.1242/dev.047753.
URL http://dx.doi.org/10.1242/dev.047753

[85] O. Biehlmaier, S. Neuhauss, K. Kohler, Onset and time course of apoptosis in the developing zebrafish retina, Cell and Tissue Research 306 (2) (2001) 199–207. doi:10.1007/s004410100447.
URL http://link.springer.com/10.1007/s004410100447

[86] J. Bezanson, A. Edelman, S. Karpinski, V. B. Shah, Julia: A Fresh Approach to Numerical Computing, SIAM Review 59 (1) (2017) 65–98. doi:10.1137/141000671.
URL https://epubs.siam.org/doi/10.1137/141000671

[87] J. Schindelin, I. Arganda-Carreras, E. Frise, V. Kaynig, M. Longair, T. Pietzsch, S. Preibisch, C. Rueden, S. Saalfeld, B. Schmid, J.-Y. Tinevez, D. J. White, V. Hartenstein, K. Eliceiri, P. Tomancak, A. Cardona,

Fiji: an open-source platform for biological-image analysis., Nature Methods 9 (7) (2012) 676–682. doi:10.1038/nmeth.2019.
URL http://dx.doi.org/10.1038/nmeth.2019

[88] J. Ollion, J. Cochennec, F. Loll, C. Escudé, T. Boudier, TANGO: a generic tool for high-throughput 3D image analysis for studying nuclear organization., Bioinformatics 29 (14) (2013) 1840–1841. doi:10.1093/bioinformatics/btt276.
URL http://dx.doi.org/10.1093/bioinformatics/btt276

[89] B. Schmid, J. Schindelin, A. Cardona, M. Longair, M. Heisenberg, A high-level 3D visualization API for Java and ImageJ., BMC Bioinformatics 11 (2010) 274. doi:10.1186/1471-2105-11-274.
URL http://dx.doi.org/10.1186/1471-2105-11-274

[90] H. Akaike, A new look at the statistical model identification, IEEE Transactions on Automatic Control 19 (6) (1974) 716–723. doi:10.1109/TAC.1974.1100705.
URL http://ieeexplore.ieee.org/document/1100705/

[91] J. L. Doob, The Limiting Distributions of Certain Statistics, The Annals of Mathematical Statistics 6 (3) (1935) 160–169, publisher: Institute of Mathematical Statistics.
URL http://www.jstor.org/stable/2957546

[92] N. Metropolis, S. Ulam, The Monte Carlo method., Journal of the American Statistical Association 44 (247) (1949) 335–341. doi:10.2307/2280232.
URL http://www.jstor.org/stable/2280232?origin=crossref

[93] C. Guo, J. Peng, C. Li, Total Least Squares Algorithms for Fitting 3D Straingh Lines, International Journal of Applied Mathematics and Machine Learning 6 (1) (2017) 35–44. doi:10.18642/ijamml_7100121818.
URL http://scientificadvances.co.in/admin/img_data/1155/images/IJAMML7100121818CuipingGuo.pdf

[94] S. Bolte, F. P. Cordelières, A guided tour into subcellular colocalization analysis in light microscopy., Journal of Microscopy 224 (Pt 3) (2006) 213–232. doi:10.1111/j.1365-2818.2006.01706.x.
URL http://dx.doi.org/10.1111/j.1365-2818.2006.01706.x

[95] C. Hsiao, M. Liu, R. Stanton, M. McGee, Y. Qian, R. H. Scheuermann, Mapping cell populations in flow cytometry data for cross-sample comparison using the Friedman-Rafsky test statistic as a distance measure, Cytometry. Part A: The Journal of the International Society for Analytical Cytology 89 (1) (2016) 71–88. doi:10.1002/cyto.a.22735.

[96] J. H. Friedman, L. C. Rafsky, Multivariate Generalizations of the Wald-Wolfowitz and Smirnov Two-Sample Tests, The Annals of Statistics 7 (4) (1979) 697–717. doi:10.1214/aos/1176344722.
URL http://projecteuclid.org/euclid.aos/1176344722

[97] K. P. Burnham, D. R. Anderson, Multimodel Inference: Understanding AIC and BIC in Model Selection, Sociological Methods & Research 33 (2) (2004) 261–304. doi:10.1177/0049124104268644.
URL http://journals.sagepub.com/doi/10.1177/0049124104268644